bioRxiv preprint doi: https://doi.org/10.1101/624528; this version posted May 1, 2019. The copyright holder for this preprint (which was not certified by peer review) is the author/funder, who has granted bioRxiv a license to display the preprint in perpetuity. It is made available under aCC-BY 4.0 International license.

Feedback inhibition and its control in an insect olfactory circuit

Authors: Subhasis Ray, Zane N. Aldworth and Mark A. Stopfer*

Author affiliation: Section on Sensory Coding and Neural Ensembles, NICHD, NIH, Bethesda, Maryland 20892 USA

Abstract

Inhibitory neurons play critical roles in regulating and shaping olfactory responses in vertebrates and invertebrates. In insects, these roles are performed by relatively few neurons that can be interrogated efficiently, revealing fundamental principles of olfactory coding. Here, with electrophysiological recordings from the locust and a large-scale biophysical model, we analyzed the properties and functions of GGN, a unique giant GABAergic neuron that plays a central role in structuring olfactory codes in the locust mushroom body. Analysis of our *in vivo* recordings and simulations of our model of the olfactory network suggests that GGN extends the dynamic range of KCs, and leads us to predict the existence of a yet undiscovered olfactory pathway. Our analysis of GGN's intrinsic properties, inputs, and outputs, *in vivo* and *in silico*, reveals basic new properties of this critical neuron and the olfactory network that surrounds it.

Introduction

Olfactory information is transformed dramatically as it travels from the periphery to higher order brain centers. Multiple types of olfactory receptor neurons may respond to a given odor with vigorous bursts of action potentials, while neurons deeper in the brain, in the pyriform cortex (vertebrates) or mushroom body (insects), may respond to the same odor with only a spike or two (Bathellier, Buhl, Accolla, & Carleton, 2008; Cang & Isaacson, 2003; Friedrich & Laurent, 2001; Laurent & Naraghi, 1994; Perez-Orive et al., 2002; Poo & Isaacson, 2009). In

* Correspondence: stopferm@mail.nih.gov

bioRxiv preprint doi: https://doi.org/10.1101/624528; this version posted May 1, 2019. The copyright holder for this preprint (which was not certified by peer review) is the author/funder, who has granted bioRxiv a license to display the preprint in perpetuity. It is made available under aCC-BY 4.0 International license.

these higher order neurons, information about odors is represented sparsely by the identities of the active neurons (population coding) and in the timing of the few spikes elicited in those neurons (temporal coding)(Gupta & Stopfer, 2014; Perez-Orive et al., 2002; Poo & Isaacson, 2009; Stettler & Axel, 2009). Many studies in vertebrates and invertebrates suggest that multiple mechanisms interact to mediate these transformations, including important inhibitory contributions from GABAergic neurons(Large et al., 2018; Large, Vogler, Mielo, & Oswald, 2016; Lin, Bygrave, de Calignon, Lee, & Miesenböck, 2014; Luna & Pettit, 2010; Palmer & Harvey, 2014; Papadopoulou, Cassenaer, Nowotny, & Laurent, 2011). Here, with intracellular recordings and a new large-scale biophysical model that includes tens of thousands of neurons and spans multiple layers of olfactory processing, we focus on a singularly important inhibitory neuron to investigate the roles of input activity and feedback inhibition in creating a sparse spatio-temporal odor representation in a higher order brain center. Together, our recordings and models point to new functions, neural connectivity patterns, and mechanisms that underlie transformations in the format of olfactory information.

The locust olfactory system is tractable owing to its relative simplicity and is well studied. At rest, olfactory receptor neurons (ORNs) are spontaneously active, evoking spontaneous activity in the antennal lobe's projection neurons (PNs; Figure 1a)(Joseph, Dunn, & Stopfer, 2012). Odorants can increase or decrease the firing rates of ORNs, and odor-elicited spikes arise in patterns that can include periods of excitation and inhibition that vary with the odor. The heterogeneous responses of ORNs drive firing patterns in PNs that are further shaped by inhibition from the antennal lobe's local interneurons (LN)(Raman, Joseph, Tang, & Stopfer, 2010). Spikes in PNs are also coaxed into rhythmic waves by fast reciprocal interactions between excitatory PNs and inhibitory LNs(Bazhenov et al., 2001; MacLeod & Laurent, 1996). Odor-elicited firing patterns distributed across the population of PNs are informative about the identity, concentration, and timing of the odor(Brown, Joseph, & Stopfer, 2005; Laurent, Wehr, & Davidowitz, 1996; Stopfer, Jayaraman, & Laurent, 2003).

bioRxiv preprint doi: https://doi.org/10.1101/624528; this version posted May 1, 2019. The copyright holder for this preprint (which was not certified by peer review) is the author/funder, who has granted bioRxiv a license to display the preprint in perpetuity. It is made available under aCC-BY 4.0 International license.

This information is carried by PNs to the mushroom body and the lateral horn. Within the mushroom body, the primary neurons are Kenyon cells (KCs). Unlike the volubly spiking PNs, the KCs are nearly silent at rest and respond very selectively to odors with very few spikes(Joseph et al., 2012; Laurent & Naraghi, 1994; Perez-Orive et al., 2002). Thus, any given odor evokes responses in a small fraction of the KC population, and any KC responds to a small set of odors(Perez-Orive et al., 2002; Stopfer et al., 2003). This sparseness of activity in KCs is thought to arise mainly from two factors: specialized membrane conductances that imbue them with high firing thresholds; and a feedback circuit that tamps down their spiking with cyclic inhibition(Demmer & Kloppenburg, 2009; Lin et al., 2014; Papadopoulou et al., 2011; Perez-Orive et al., 2002). In the locust the main source of this inhibition is the giant GABAergic neuron (GGN), one on each side of the brain(Gupta & Stopfer, 2012; Leitch & Laurent, 1996; Papadopoulou et al., 2011).

GGN spans much of each brain hemisphere and branches very widely (Figure 1a). It is reported to receive excitatory input from all 50,000 KCs at synapses within the mushroom body's α lobe and, in turn, provide inhibitory feedback to all KCs 400-500 microns away within the calyx. In addition, GGN receives inhibitory input from a spiking neuron aptly named "Inhibitor of GGN" (IG) which itself receives inhibition from GGN (Figure 1a, right)(Papadopoulou et al., 2011). GGN is a non-spiking interneuron. Odor presentations, spiking in KCs, and intracellular current injections have all been shown to depolarize GGN, but none of these stimuli causes GGN to generate spikes; even large depolarizations induced by strong intracellular current injections lead only to passive depolarizing responses(Leitch & Laurent, 1996; Papadopoulou et al., 2011) (also our own observations).

GGN's structure is likely an important factor in its function. GGN is very large, and along its path from the α lobe to the calyx, its initially thick processes divide at myriad branch points into vanishingly thin fibers. Cable theory applied to neurons(Rall, 1964) predicts that a passive voltage signal within such a structure will attenuate dramatically as it encounters cytosolic resistance along the neurites, will attenuate further as it divides at the neuronal

bioRxiv preprint doi: https://doi.org/10.1101/624528; this version posted May 1, 2019. The copyright holder for this preprint (which was not certified by peer review) is the author/funder, who has granted bioRxiv a license to display the preprint in perpetuity. It is made available under aCC-BY 4.0 International license.

arbor's branch points, and will leak out through ionic channels in the cell membrane. Together, these features made it unclear whether this giant neuron has the biophysical capacity to perform its suggested function of carrying effective signals passively from the α lobe to distant points in the calyx. Prior studies in invertebrates have shown that 2-5 mV depolarizations in nonspiking interneurons can evoke change in membrane potential of their post-synaptic neurons(Burrows & Siegler, 1978; Manor, Nadim, Abbott, & Marder, 1997). If the signal through GGN attenuates to the extent that it cannot elicit responses in KCs then GGN must operate through a different mechanism, perhaps purely through local interactions in the calyx. To test these ideas, we developed a realistic computational model of GGN to characterize signal attenuation along this pathway. Our model showed that, although electrical signals undergo substantial attenuation throughout its structure, signals in GGN's calyceal branches appear strong enough to provide global inhibition to KCs.

To further understand the network determinants of GGN's responses to odors, we recorded from it *in vivo* while delivering a variety of odors to the animal, and then used our large-scale model to investigate the types of network activity needed to generate these patterns. We identified three novel features in the olfactory network. First, to generate the types of membrane potential patterns we observed in GGN, the synaptic connection strengths onto KCs must be heterogeneous. Second, and surprisingly, our model predicted that a small portion of KCs must respond to odors with relatively high spike rates. We tested this prediction *in vivo* with patch clamp recordings from many KCs while presenting odors to the animal's antenna. Indeed, we found that the predicted portion of KCs responded to odors with relatively high rates of spiking. Third, our *in vivo* recordings of GGN revealed novel, complex response patterns not previously documented, including periods of hyperpolarization, that vary with the odorant. Although GGN receives reciprocal feedback from IG(Papadopoulou et al., 2011), the periods of hyperpolarization could not be explained by disinhibition of IG from GGN. Instead, our model predicts that this behavior could arise if,

bioRxiv preprint doi: https://doi.org/10.1101/624528; this version posted May 1, 2019. The copyright holder for this preprint (which was not certified by peer review) is the author/funder, who has granted bioRxiv a license to display the preprint in perpetuity. It is made available under aCC-BY 4.0 International license.

in addition to receiving input from GGN, IG also receives direct excitation from another, unknown odor-activated pathway.

Together, the results of our *in vivo* recordings and large-scale realistic computational modeling provide a more complete understanding of how different parts of the olfactory system interact. To generate odor-specific temporally patterned responses in GGN and in the mushroom body, temporally-patterned odor evoked excitation from PNs, feedback inhibition from GGN, and inhibition of GGN by odor-driven IG must all cooperate. Further, to sustain adequate activity in GGN, some KCs must respond to odors with relatively high spike rates.

Results

GGN morphology

A valuable use of computational modeling is to answer questions about biological systems that are too large, complex, or difficult to address by direct physiological investigation. Earlier computational studies of the insect olfactory system used relatively simple models of neurons such as integrate and fire or map-based models that collapse entire neuronal structures into a single point(Arena, Calí, Patané, Portera, & Strauss, 2015; Kee, Sanda, Gupta, Stopfer, & Bazhenov, 2015; Papadopoulou et al., 2011; Peng & Chittka, 2017; Perez-Orive, Bazhenov, & Laurent, 2004). However, GGN's giant size, elaborate branching, and passive membrane properties raised questions about its function that could only be addressed by considering properties determined by its morphology. Thus, to understand how the size and shape of GGN affects electrical signal propagation, we constructed a detailed morphological model of GGN (available at neuromorpho.org).

To reconstruct the morphology of GGN we first made intracellular recordings from it *in vivo*, filled it with dye, and obtained 3D confocal images of the dye-filled cell (Figure 1a, left; Video S1). As previously shown, GGN has a reliable and unique location and morphology(Gupta & Stopfer, 2012; Leitch & Laurent, 1996; Papadopoulou et al., 2011). Its soma is on the ventral

bioRxiv preprint doi: https://doi.org/10.1101/624528; this version posted May 1, 2019. The copyright holder for this preprint (which was not certified by peer review) is the author/funder, who has granted bioRxiv a license to display the preprint in perpetuity. It is made available under aCC-BY 4.0 International license.

side of the brain, just anterior to the optic nerve. A single neurite emerges from GGN's soma, travels toward the posterior and dorsal side of the brain, and splits there into two branches, one innervating the α lobe and the other the mushroom body. Extending outward, these branching neurites expand in width, becoming much thicker than the primary neurite. The mushroom body branch further divides into two thick processes that innervate the medial and the lateral calyx. A thin neurite emerging from the lateral calyceal branch loops back to the lateral horn, close to the soma, and splits there into many branches. We further observed for the first time myriad thin fibers that emerge from the stems of the calyceal branches and split into very fine feather-like neurites that wrap densely around the peduncle, with some investing the peduncle core (Figure 1b). The neurites in the calyx and lateral horn are dotted with many irregular bouton-like structures (Figure 1c) whereas the branches in α lobe are relatively smooth (Figure 1d).

In two animals we traced and reconstructed the morphology of GGN from confocal image stacks (Figure 1e). Analyzing these traces, we found that the maximum path length (i.e., the maximum distance between any two points on the neuronal tree when traversed along the neurites) of the neuronal trees was on the order of 2mm, and the maximum physical length (i.e., Euclidean distance between any two points on the neuron in three-dimensions) was on the order of 1mm. Some neurites at their thickest were nearly 20μm in diameter. Total traced branch length (i.e., the sum of the lengths of all the neurites) was about 65mm (although many vanishingly thin branches were too fine to trace). Compared to 96,831 vertebrate and invertebrate neurons cataloged in the neuromorpho.org database, GGN fell into the 99.75th percentile for total branch length, and the 99.95th percentile for number of branch points. It is a really big neuron.

Signal attenuation in GGN

To investigate GGN's electrical properties we constructed a passive electrical model cell by transferring the morphology tracings of the two GGNs into the NEURON

bioRxiv preprint doi: https://doi.org/10.1101/624528; this version posted May 1, 2019. The copyright holder for this preprint (which was not certified by peer review) is the author/funder, who has granted bioRxiv a license to display the preprint in perpetuity. It is made available under aCC-BY 4.0 International license.

simulator(Carnevale & Hines, 2006). Both models produced qualitatively similar results; the model we describe here was derived from the second neuron we traced because it was imaged at higher resolution. To account for branches and changes in the diameters of processes that affect electrotonic distance we segmented the model GGN into 5,283 compartments. We set the membrane resistivity in the model to 33 kohm-cm^2 based on published data obtained from other non-spiking neurons in the locust(Laurent, 1991), the specific membrane capacitance to 1 μF/cm^2, the approximate value for cell membranes(Curtis & Cole, 1938; Gentet, Stuart, & Clements, 2000; Hodgkin & Huxley, 1952) and the cytoplasmic resistivity to 100 ohm-cm, a typical order-of-magnitude value for neurons(Hodgkin & Rushton, 1946; Roth & Häusser, 2001; Stuart & Spruston, 1998).

Feedback signals are thought to travel passively from GGN's α lobe branch to its calyceal branches. To test the extent of passive signal attenuation through GGN's structure, we first simulated voltage clamping the base of the α lobe branch of the GGN model (Figure 2a). Intracellular recordings(Papadopoulou et al., 2011) (and our own) show GGN's membrane potential rests at about -51 mV. Because strong odor stimuli depolarize GGN by about 10 mV in recordings made near the base of the α lobe branch(Papadopoulou et al., 2011) (also see Figure 5a) we first stepped the clamp voltage to -40 mV and after holding it there for 450 ms measured the resulting depolarizations throughout the model GGN (Figure 2a inset). Notably, the extent of signal attenuation was substantial and varied throughout the calyx with depolarizations ranging from ~5 - 9 mV. The signal decreased with branch distance from the α lobe, leaving the least amount of signal at the medial portion of the lateral calyceal branch (Figure 2b, c, Video S2).

Since excitatory input typically arrives in GGN from many KCs, we then tested a more realistic form of simulated input to the α lobe arbor of GGN by providing nonhomogeneous Poisson spike trains through 500 excitatory model synapses; each synapse had a maximum rate of 20 spikes/s that ramped down linearly to 0 over a 500 ms interval (Figure 2d, e). This

bioRxiv preprint doi: https://doi.org/10.1101/624528; this version posted May 1, 2019. The copyright holder for this preprint (which was not certified by peer review) is the author/funder, who has granted bioRxiv a license to display the preprint in perpetuity. It is made available under aCC-BY 4.0 International license.

stimulus set was calibrated to generate a peak depolarization in the thick branches of GGN in the same range we observed *in vivo*. This test also revealed significant attenuation of voltage in the neuron's distant branches (Figure 2e, f).

For GGN neither membrane resistivity (RM) nor cytoplasmic (axial) resistivity (RA) has been measured definitively; yet, for a given morphology, these two parameters determine signal attenuation. Thus, we explored a range of values for these two parameters with the voltage clamp simulation approach shown in Figure 2a. We based the RM value range on data obtained from many types of neurons provided by the neuroelectro.org database. For RA, neurophysiological data is sparse, so we explored broadly around the range of published values(Hodgkin & Rushton, 1946; Roth & Häusser, 2001; Stuart & Spruston, 1998). As expected, higher RA yielded greater signal attenuation, whereas higher RM yielded less signal attenuation (Figure 2g). This analysis showed that signal transmission in GGN is robust; except for the most extreme values of this parameter range, signals from the α lobe remained strong enough to support synaptic transmission in the calyx. Depolarization throughout GGN's calyceal arbor varied with location, as quantified in the extended lower lobe in the violin plots in Figure 2c, f and g.

Branches of GGN receiving weaker signals would be expected to provide less inhibition to their postsynaptic KCs. In a simplified model in which all KCs were strongly stimulated by identical input from PNs, the amount of KC spiking was indeed negatively correlated with local GGN voltage deflections (Figure S3). However, in a more realistic model of the mushroom body network including variable excitatory input from PNs and variable strengths of inhibitory synapses between GGN and KCs, we found the negative correlation between depolarizations measured at presynaptic locations throughout GGN and postsynaptic KC activity was small, and likely negligible (data not shown). This suggests GGN's inhibitory output has a surprisingly uniform influence upon KCs regardless of their locations.

bioRxiv preprint doi: https://doi.org/10.1101/624528; this version posted May 1, 2019. The copyright holder for this preprint (which was not certified by peer review) is the author/funder, who has granted bioRxiv a license to display the preprint in perpetuity. It is made available under aCC-BY 4.0 International license.

Feedback inhibition expands the dynamic range of KCs

Feedback inhibition from GGN sparsens the odor-elicited responses of KCs by increasing the KC spiking threshold and by restricting KC spiking to brief temporal windows defined by the oscillatory cycle established in the AL(Gupta & Stopfer, 2014; Papadopoulou et al., 2011). Large-scale feedforward inhibition has previously been shown to expand the dynamic range of cortical neurons(Pouille, Marin-Burgin, Adesnik, Atallah, & Scanziani, 2009). Whether feedback inhibition from GGN has a similar effect on KCs is unknown. To test this, we expanded our model to include, for simplicity, a single KC receiving feedback inhibition from GGN (Figure 3a). To simulate the KC in this test we used a single compartmental model with Hodgkin-Huxley type ion channels(Wüstenberg et al., 2004). Since just one KC would have negligible effects on GGN, we applied its spiking output to GGN's α lobe branch via 50,000 synapses, each with random delays between 0 and 60ms. Thus, after each spike generated by the model KC, GGN received 50,000 EPSPs spread over a 60ms time window. We drove the KC model with a range of tonic current injections and compared its responses to those of an isolated KC model receiving the same input without feedback inhibition. As expected, feedback inhibition increased the KC's threshold for spiking. Notably, though, the GGN-coupled KC continued to spike over a much larger range of current injection than the isolated KC, which quickly saturated to a level where it could no longer spike (Figure 3b, c). This result suggests that feedback inhibition from GGN allows an individual KC to function effectively over a larger dynamic range of inputs.

GGN responses can be complex, including hyperpolarization

Our recordings made *in vivo* from GGN frequently revealed depolarizations lasting throughout an odor presentation, often with additionally depolarizing peaks corresponding to the onset and offset of the odor (Figure 4, Animal 1, hexanol) (see also(Papadopoulou et al., 2011)). Notably, our recordings from GGN also revealed more complex odor-elicited responses than previously reported, including combinations of depolarization and hyperpolarization (Figure 4, Animal 1, hexanal). Moreover, we found that the same GGN

bioRxiv preprint doi: https://doi.org/10.1101/624528; this version posted May 1, 2019. The copyright holder for this preprint (which was not certified by peer review) is the author/funder, who has granted bioRxiv a license to display the preprint in perpetuity. It is made available under aCC-BY 4.0 International license.

could respond differently when different odors were presented; for example, GGNs from Animals 2 and 3 shown in Figure 4 depolarized in response to one odor and hyperpolarized in response to another. Also, GGNs in different animals could respond differently to the same odor (Figure 4, hexanal). Almost a quarter of the odor-GGN pairs in our *in vivo* recordings showed reliable hyperpolarizations at some point in the odor response (40 out of 169). However, earlier computational models(Kee et al., 2015; Papadopoulou et al., 2011) did not reproduce sustained responses in GGN, nor did they show any hyperpolarization of GGN. Rather, in those models, odor-driven KCs spiking in synchronous bouts elicited multiple isolated depolarizing peaks in GGN's membrane potential. To better understand the mechanisms underlying GGN's odor-elicited responses (and by extension, novel features of olfactory circuitry), we used our GGN model as the center of a more extensive mushroom body olfactory network.

GGN responses suggest some KCs fire at high rates

We extended our detailed GGN model with a full population of 50,000 simulated KCs. KCs are very small, have few dendritic branches, and generate action potentials; thus, in contrast to the large, complex, and passive GGN, the morphologies of individual KCs are unlikely to differentially influence their odor coding properties. Therefore, we used a relatively simple NEURON version of a single compartmental KC model(Wüstenberg et al., 2004). Each model KC was connected to GGN in the α lobe via an excitatory synapse, and each received inhibitory input from a random segment of GGN in the calyx via a graded synapse (Figure 5a). To provide excitatory input to the KCs, the firing patterns of 830 PNs were simulated as spike-trains, each designed to follow the statistics of PNs recorded *in vivo*(Jortner, Farivar, & Laurent, 2007; Mazor & Laurent, 2005). Thus, 77% of the PN spike trains were assigned a spontaneous firing rate of 2.6 spikes/s; during odor stimulation, 20% of these PNs were switched to 20 spikes/s modulated by the 20 Hz oscillations generated in the antennal lobe and reflected in the local field potential (LFP), and 10% were inhibited (no spikes) (Figure 5b). This resulted in a few highly synchronized bouts of spiking in the KC

bioRxiv preprint doi: https://doi.org/10.1101/624528; this version posted May 1, 2019. The copyright holder for this preprint (which was not certified by peer review) is the author/funder, who has granted bioRxiv a license to display the preprint in perpetuity. It is made available under aCC-BY 4.0 International license.

population (Figure 5c), and corresponding isolated peaks in GGN's membrane potential (Figure 5d). These unrealistic responses were similar to those generated by the above-mentioned earlier models.

We suspected that more continuous input from KCs could sustain the long-lasting depolarization in GGN we had observed *in vivo*. In our model all synapses between any two cell types had the same strength. However, it has been shown *in vivo* that synaptic strengths follow a lognormal distribution(Buzsáki & Mizuseki, 2014; Loewenstein, Kuras, & Rumpel, 2011; Song, Sjöström, Reigl, Nelson, & Chklovskii, 2005). After adjusting our network model to include this property, some KCs became weakly inhibited, allowing them to fire more volubly. Also in our model, input to the KCs emulated a fixed set of PNs constantly active throughout the duration of the odor stimulus. However, *in vivo*, spiking patterns of PNs evolve over the course of an odor presentation, and different PNs respond to the same odor in different ways(Laurent & Davidowitz, 1994; Mazor & Laurent, 2005; Stopfer et al., 2003), thus activating changing sets of KCs. To simulate these diverse responses, we divided the model's PN population into five groups: four groups responsive to the stimulus and one unresponsive. Odor-elicited spiking within each of the responsive groups started in a subset of its member PNs, and then, in each successive LFP cycle, new PNs were activated (Figure 5e). Lacking the heterogeneity in synaptic strengths onto KCs described above, even this complex activity pattern in PN population produced unrealistically synchronized bouts of activity in KCs, resulting in unrealistic isolated peaks in GGN's simulated membrane potential (Figure 5f). However, we found that combining heterogeneous connectivity with structured PN firing patterns gave rise to GGN voltage traces that included sustained depolarization and temporal dynamics more characteristic of responses we had observed *in vivo* (Figure 5g). The distribution of firing rates of the KC population showed that, while most KCs produced 0-2 odor-elicited spikes, a few KCs spiked much more (Figure 5h). Thus, our analysis of GGN's voltage profile led us to predict that a few odor responses in KCs are far more intense.

bioRxiv preprint doi: https://doi.org/10.1101/624528; this version posted May 1, 2019. The copyright holder for this preprint (which was not certified by peer review) is the author/funder, who has granted bioRxiv a license to display the preprint in perpetuity. It is made available under aCC-BY 4.0 International license.

To test this *in vivo*, we made patch clamp recordings from 147 KCs in 114 animals, obtaining results from 707 KC-odor pairs. On average, the spontaneous firing rates of these KCs were very low (~0.09 Hz) and reached only somewhat higher rates during and after odor termination (~0.15 and ~0.16 Hz, respectively, Figure 6a), as previously observed(Gupta & Stopfer, 2014; Perez-Orive et al., 2002). Notably, though, we also found that some odor-elicited responses in KCs consisted of many more spikes. Figure 6b shows a representative example of a hyperactive KC response, in which a 1s odor pulse elicited an average of 7 spikes (Figures 6c and d). Overall, the distribution of spike counts in KCs we tested was clustered close to 0 but included a long rightward tail (Figure 6e), in striking agreement with our prediction (Figure 5h). This result expands our view of KC activity to include a broader range of odor-elicited spiking.

Odor evoked spiking in IG can explain GGN hyperpolarization

Our intracellular recordings from GGN revealed extended periods of odor-elicited hyperpolarization (Figure 4), something not previously observed nor explainable by existing models of GGN within its olfactory network. We hypothesized that these periods of hyperpolarization might originate in the activity of IG, a neuron known to share reciprocal inhibition with GGN (Figure 1a, right)(Papadopoulou et al., 2011). Specifically, we hypothesized that an increase in IG activity might underlie the periods of hyperpolarization in GGN, with IG's activity increase caused by disinhibition from GGN. To test this, we first tried adding a simple version of IG to our model following the reciprocal connectivity plan shown in Figure 1a. But, despite testing a broad range of IG properties, this configuration could not generate odor-elicited hyperpolarization in GGN (data not shown). Something more was needed.

The location and most properties of IG are unknown, and we were not able to identify it in our recordings. However, a previous report showed spikes in IG correlate one-to-one with IPSPs in GGN(Papadopoulou et al., 2011), suggesting we could infer IG's activity by examining GGN's membrane potential. Our recordings made *in vivo* from GGN revealed an

bioRxiv preprint doi: https://doi.org/10.1101/624528; this version posted May 1, 2019. The copyright holder for this preprint (which was not certified by peer review) is the author/funder, who has granted bioRxiv a license to display the preprint in perpetuity. It is made available under aCC-BY 4.0 International license.

odor-elicited increase in the frequency of IPSPs in GGN's membrane potential (Wilcoxon signed-rank test, N=198 pairs, W=2328.5, $p << 0.001$); responses from 2 animals are shown in Figure 7a, and responses from 1257 trials with several odors from 47 GGNs are shown as a peri-stimulus time histogram in Figures 7b and c. Assuming these IPSPs originate as spikes in IG(Papadopoulou et al., 2011), these results show that IG is spontaneously active, and that its responses to an odor pulse are delayed and lengthy. Further, as evident in Figure 7b, IG's firing rate begins to increase before GGN's membrane potential returns to baseline, suggesting that IG's odor response cannot be driven by disinhibition from GGN. Therefore, we hypothesized that IG receives its odor-elicited excitatory synaptic input via a different odor-driven pathway, for example, from PNs or KCs. Using our model, we could indeed reproduce realistic hyperpolarization in GGN's membrane potential by adding excitatory synapses to IG from either the PNs or the KCs (Figures 7d and e). Depending on the PN activity pattern, our simulations produced GGN membrane potentials with hyperpolarization and depolarization (Figure 7e-g).

A remaining question concerned the source of excitation driving spontaneous activity in IG (Figure 7h, top black traces). KCs are nearly silent at rest(Gupta & Stopfer, 2014; Perez-Orive et al., 2002), ruling them out as the sole source of excitation to IG. PNs, though, spike spontaneously because they receive direct, powerful input from spontaneously active ORNs(Joseph et al., 2012), suggesting a PN-driven pathway might be responsible for spontaneous activity in IG. To test this *in vivo*, we completely silenced PNs and KCs by bilaterally cutting the animal's antennal nerves(Joseph et al., 2012) and then recorded intracellularly from GGN. We found that spontaneous IPSPs in GGN persisted as normal in preparations with silenced PNs and KCs (Figure 7h, bottom red traces), demonstrating that IG's spontaneous spiking either arises intrinsically or is driven by a source other than PNs or KCs.

bioRxiv preprint doi: https://doi.org/10.1101/624528; this version posted May 1, 2019. The copyright holder for this preprint (which was not certified by peer review) is the author/funder, who has granted bioRxiv a license to display the preprint in perpetuity. It is made available under aCC-BY 4.0 International license.

Discussion

Inhibitory neurons play critical roles in regulating and shaping olfactory responses in vertebrates and invertebrates(Kay & Stopfer, 2006). In insects, these roles are performed by relatively few neurons that can be interrogated efficiently, revealing fundamental principles of olfactory coding. The unique giant GABAergic neuron GGN plays a central role in structuring olfactory codes in the locust mushroom body by regulating the excitability of KCs and parsing their responses into rhythmic bursts. We combined intracellular recordings from GGN and KCs, and developed a new morphologically detailed model of GGN as a focus of analysis to investigate GGN's properties, inputs, and outputs. Further, we used a broader model of the olfactory system built around GGN to explore several basic properties of the olfactory network. Our new electrophysiological recordings and computational model successfully reproduced the sparse activity of KCs and the membrane dynamics of GGN in the locust brain while providing concrete hypotheses about how the mushroom body circuit may process odor information.

Non-spiking interneurons in insects are often large with complex splays of neurites in separate brain areas, suggesting their far-flung branches may be functionally isolated, serving separate local computations(Burrows, 1981). It has been proposed that signals generated within GGN's α lobe branch propagate to its calyceal branch, where they transmit global inhibition to all KCs(Papadopoulou et al., 2011). But, the enormous size, extensive branching, and passive conduction characterizing GGN raised the hypothesis that GGN's α lobe signals would attenuate to such an extent as they travel to the calyx that they would be unable to effectively inhibit KCs. Our simulation of GGN's morphological and electrical properties suggests that realistic levels of depolarizations of 10mv in GGN's α lobe branch do indeed attenuate greatly with distance to amplitudes as low as 5mv in parts of the calyx. However, earlier studies of non-spiking neurons in invertebrates showed depolarizations of this amplitude should suffice to evoke neurotransmitter release. For example, (Burrows & Siegler, 1978) showed that depolarizations of only about 2 mV in a non-spiking interneuron

bioRxiv preprint doi: https://doi.org/10.1101/624528; this version posted May 1, 2019. The copyright holder for this preprint (which was not certified by peer review) is the author/funder, who has granted bioRxiv a license to display the preprint in perpetuity. It is made available under aCC-BY 4.0 International license.

in the metathoracic ganglion of the locust suffices to change the firing rate of its postsynaptic motor neuron. Similarly, (Manor et al., 1997) showed in a graded synapse in the lobster stomatogastric ganglion that voltage steps from -50 mV to -45 mV can reliably evoke postsynaptic effects. Thus, we conclude that input from KCs at GGN's α lobe branches could provide effective global inhibition to all KCs in the calyx.

GGN's arborizations in the calyx extend different lengths, suggesting signals arising in the α lobe could attenuate more in some of its calyceal branches than in others. Our simulations indeed showed the amount of depolarization reaching GGN's distant branches varied with their locations, but only by a few millivolts (Figure 2b). Perhaps consistent with this, APL, the *Drosophila* analog of GGN(Lin et al., 2014) appears to provide varying levels of feedback inhibition to different groups of KCs(Inada, Tsuchimoto, & Kazama, 2017). Odor-elicited responses of KCs result from non-linear combinations of many factors in addition to the amount of depolarization reaching presynaptic terminals of GGN; these factors include the KCs' intrinsic properties, excitatory input from PNs, and the strengths of inhibitory synapses from GGN. Thus, although we observed variations in the amplitudes of GGN depolarization in our model's calyceal branches, they did not appear to contribute significantly to variations in KC excitability. For example, KCs in the medial calyx did not consistently spike more than KCs in lateral areas.

Our model does not address the possibility that local, reciprocal connectivity between GGN and KCs might occur in the calyx alongside global inhibition. In *Drosophila*, APL is known from electron microscope image reconstructions to receive synapses from KCs in the calyx, possibly enabling local feedback(Eichler et al., 2017; Zheng et al., 2018). If KCs make reciprocal local connections with GGN within the calyx along with convergent connections in the α lobe, then the relative influence of global and local inhibition might vary with stimulus intensity. We speculate that very weak olfactory stimuli that minimally activate KCs will evoke in the α lobe branch of GGN only small depolarizations which would attenuate below threshold upon reaching the calyx. This would allow local inhibition to dominate, consistent

bioRxiv preprint doi: https://doi.org/10.1101/624528; this version posted May 1, 2019. The copyright holder for this preprint (which was not certified by peer review) is the author/funder, who has granted bioRxiv a license to display the preprint in perpetuity. It is made available under aCC-BY 4.0 International license.

with recent observations in the *Drosophila* mushroom body circuit(Inada et al., 2017). In this local inhibition scenario, a spiking KC would effectively inhibit only its close neighbors via GGN. Combined with random connectivity from PNs, this circuitry might result in a winner-take-all, center-surround-type of contrast enhancement in which only the most strongly driven KCs in each region of GGN's arbor can respond to an odor. On the other hand, in the case of very strong olfactory stimuli (or in the absence of local KC-GGN reciprocal connections in the calyx), global inhibition will dominate and KCs receiving inhibition from the same region of GGN would likely fire together, reducing the contrast among their response.

Inhibition from GGN is known to sparsen the firing of KCs and to impose rhythmic time windows on their responses(Gupta & Stopfer, 2012; Papadopoulou et al., 2011). Notably, our model also revealed that feedback inhibition from GGN can expand the range of inputs able to activate KCs (Figure 3). We found our isolated model KCs only generated spikes when stimulated by a narrow range of current; too little current failed to evoke any response, and too much current was saturating (Figure 3). In the real brain, a wide range of synaptic strengths exists even within a given type of neuron, and synaptic strength can change over time and with experience (reviewed in(Barbour, Brunel, Hakim, & Nadal, 2007)). It is possible that ionic conductances in KCs are precisely and constantly tuned by homeostatic mechanisms to match their inputs, enabling them to respond appropriately to a broad and changing range of inputs (reviewed in(Marder & Goaillard, 2006)). Our results suggest that feedback inhibition may also help KCs function robustly by expanding their sensitivities to a wider range of inputs, enabling them to generate consistently sparse responses.

Our intracellular recordings from GGN often revealed odor-elicited periods with sustained depolarization (Figure 4), a response feature unexplainable by existing models. What inputs underly GGN's membrane potential? KCs, which provide excitation to GGN, have been shown to respond very sparsely to any given odor, with very few cells firing just one or a few spikes(Laurent & Naraghi, 1994; Mazor & Laurent, 2005; Perez-Orive et al., 2004). Our simulations showed that sparse spiking in the entire KC population cannot generate the

bioRxiv preprint doi: https://doi.org/10.1101/624528; this version posted May 1, 2019. The copyright holder for this preprint (which was not certified by peer review) is the author/funder, who has granted bioRxiv a license to display the preprint in perpetuity. It is made available under aCC-BY 4.0 International license.

large sustained depolarizations we observed *in vivo* in GGN. When we adjusted the excitatory and inhibitory inputs to the KCs to generate a few spikes upon activation of a fixed set of PNs by odorant, the KC population responded with unrealistically strong bursts of synchronous activity, resulting in unrealistic prominent peaks in GGN's membrane potential. Simply increasing the excitability of KCs in a network driven by odor-evoked oscillatory spiking in a fixed set of PNs succeeded in generating realistic GGN responses, but also elicited spiking in an unrealistically large number of KCs in the model. We found we could solve this problem by introducing variability in the strength of the synapses onto KCs (Figure S4). Further, when we drove KCs with more realistic, heterogeneous patterns of excitatory input from PNs, the resulting responses of GGN and the KC population generally matched our observations *in vivo* (Figure 5). Notably, close inspection of the revised model's KC odor response distribution revealed a small subset of responses with more spiking than had previously been documented, thus predicting some KC responses *in vivo* are much stronger than previously reported. Notably, our patch recordings from neurons confirmed to be KCs by dye fills revealed the predicted distribution of responsiveness (Figure 6e). KCs generating especially strong responses were not localized in any particular part of the calyx, nor did they feature distinguishing morphologies (data not shown). It is unclear why hyperactive KC responses were not previously observed in the locust mushroom body, but one possibility is that unusually active neurons recorded here (but not filled) were misidentified as other cell types. This small group of over-active KC responses appears to play a key role in olfactory processing by driving sustained global inhibition.

Our intracellular recordings from GGN also revealed more elaborate membrane potential temporal dynamics than previously reported, including prolonged stimulus-dependent periods of hyperpolarization, that varied with odor and animal. In our model, simple reciprocal inhibition of GGN by the inhibitory neuron IG could not reproduce these features. Rather, realistic hyperpolarization of GGN's membrane potential could be caused by odor-elicited activity in the inhibitory neuron IG (Figure 8). The direct source of odor-elicited

bioRxiv preprint doi: https://doi.org/10.1101/624528; this version posted May 1, 2019. The copyright holder for this preprint (which was not certified by peer review) is the author/funder, who has granted bioRxiv a license to display the preprint in perpetuity. It is made available under aCC-BY 4.0 International license.

excitatory drive to IG is unknown, but could, in principle, be traced to KCs. Indeed, a version of our model in which all KCs synapse upon IG reliably reproduced realistic odor-elicited hyperpolarizations in GGN. Why are these hyperpolarizations elicited by only some odors in some animals, as we saw *in vivo* (Figure 4)? Our simulations suggest that odor-specific temporal pattern in the PN population's response(Stopfer et al., 2003) can explain this phenomenon (Figure 7e-g).

In summary, we used biophysically detailed simulations in combination with *in vivo* electrophysiology to explore the olfactory circuit in the locust mushroom body. Our intracellular and patch recordings revealed new features of GGN, a neuron that plays a central role in shaping olfactory responses, and of the KC population, which we show to generate a small subset of hyperactive responses, as predicted by our model. These results extend our understanding of the olfactory system, highlighting ways different components interact, and providing new predictions for additional research.

Materials and Methods

Dissection and electrophysiology

Newly eclosed adult locusts of both sexes picked randomly from our crowded colony were immobilized and the brain was exposed, desheathed and superfused with locust saline as described before(Brown et al., 2005). No sample size estimation was done beforehand. As this was an exploratory study and odor response was specific to each GGN and odor, we tried to collect data from as many animals as we could. We commonly obtained recordings from one GGN in each animal, mostly one in a day, over a year. The results were similar months apart. To record from GGN, a sharp glass micropipette filled with 2 or 3M potassium acetate with 5% neurobiotin was inserted into the peduncle region of the mushroom body; when impaled, GGN could be identified by its characteristic pattern of IPSPs in the voltage record (Figure 7h). At the end of the recording session, neurobiotin was injected into the cell

bioRxiv preprint doi: https://doi.org/10.1101/624528; this version posted May 1, 2019. The copyright holder for this preprint (which was not certified by peer review) is the author/funder, who has granted bioRxiv a license to display the preprint in perpetuity. It is made available under aCC-BY 4.0 International license.

iontophoretically using 0.2 nA current pulses at 3 Hz for 10 to 20 minutes, and the cell's identity was confirmed by subsequent imaging.

To test whether IPSPs in GGN originate from spontaneous activity in PNs, we first silenced the PNs by cutting both antennal nerves at the base(Joseph et al., 2012) and then searched for GGN, which could still be identified by its pattern of IPSPs and by its morphology, revealed by subsequent filling with neurobiotin and imaging.

For patch clamp recordings from KCs, the initial dissection was performed as described above. Patch pipettes were pulled to between 7 and 12 MΩ, filled with locust internal solution(Laurent, Seymour-Laurent, & Johnson, 1993) as well as a neural tracer for subsequent histology (either 12 mM neurobiotin for later conjugation with an Avidin-Alexa complex, or 20 µM Alexa Fluor tracer with absorption wavelengths of 488, 568 or 633). Patch recordings were made in current clamp mode, and data was only analyzed if the observed membrane potential was within the previously reported range for KCs (-55 to -65 mV) and if either LFP or membrane potential oscillations were observed in response to odor stimulation. Firing rates were obtained by smoothing the PSTH with a 100 ms SD gaussian window.

Stimulus delivery

For GGN recordings, odor pulses were delivered to the ipsilateral antenna as described in (Gupta & Stopfer, 2012).The odorants included 1-hexanol at dilutions of 1% v/v, 1-hexanol, hexanal, methyl benzoate, benzaldehyde, and cyclohexanone mixed at the dilution of 10% v/v in mineral oil, and 100% mineral oil.

For KC recordings, the following odors were delivered similarly: 1-hexanol, hexanal, cyclohexanol, 1-octananol, citral, geraniol, ethyl butyrate, 1-butanol, benzaldehyde, eugenol,

bioRxiv preprint doi: https://doi.org/10.1101/624528; this version posted May 1, 2019. The copyright holder for this preprint (which was not certified by peer review) is the author/funder, who has granted bioRxiv a license to display the preprint in perpetuity. It is made available under aCC-BY 4.0 International license.

3-methyl-2-butenol, methyl jasmonate, decanal, methyl salicylate, linalool, limonene, pentyl acetate, (all 10% v/v in mineral oil, except methyl salicylate and limonene, at 40% each) and 100% mineral oil.

Histology and immunostaining

Brains were dissected from the head capsule and fixed in 4% paraformaldehyde overnight, then conjugated with Avidin-Alexa 568 or Avidin-Alexa 488. Some brains were first immunostained with mouse nc82 primary antibody (DSHB Cat# nc82, RRID:AB_2314866, deposited to the DSHB by Buchner, E.) and Alexa 568 conjugated anti-mouse IgG secondary antibody(Shimizu & Stopfer, 2017).

Imaging and neuronal tracing

Brains were dehydrated in an ethanol series and cleared with methyl salicylate or CUBIC(Susaki et al., 2014), mounted in methyl salicylate or mineral oil respectively, and imaged with a Zeiss LSM 710 confocal microscope. Two GGNs were traced in detail from 3D image stacks using NeuroLucida software (MBF Bioscience, Williston, Vermont). The traces were converted to SWC format for further processing and cleanup using NLMorphologyConverter (www.neuronland.org). The two traces were very similar; the one obtained at higher resolution was used for reconstruction and modeling.

Statistics

For each of 198 GGN-odor pairs, average spike rates were calculated over 5 trials in windows beginning 2 s before, and 2 s after, odor presentations. Wilcoxon-signed rank tests from scipy package were used to compute the statistic and the two-sided *p*-value.

bioRxiv preprint doi: https://doi.org/10.1101/624528; this version posted May 1, 2019. The copyright holder for this preprint (which was not certified by peer review) is the author/funder, who has granted bioRxiv a license to display the preprint in perpetuity. It is made available under aCC-BY 4.0 International license.

Computational model

GGN morphologies in SWC format were imported into NEURON and converted into passive models in NEURON's hoc format. The single compartmental KC model reported by (Wüstenberg et al., 2004) was translated manually into a NEURON model. The resting membrane potential was set to -51 mV, as we have observed *in vivo*. The passive reversal potential of the KCs was set to -70 mV. Custom Python scripts were written to set up network models and simulation experiments using NEURON's Python interface. The simulations were run on NIH's Biowulf supercomputer cluster (*http://hpc.nih.gov*) and simulation results were saved in HDF5 based NSDF format(Ray, Chintaluri, Bhalla, & Wójcik, 2015) and later analyzed with custom Python scripts.

PN activity model with a fixed responsive population

Modeled PN spike train rates were based on firing statistics reported in Figure 2c-e in this publication: [7] from which we infer 77% of PNs are spontaneously active. Odor presentations were set to evoke spiking in ~20% of PNs, each spiking at an average rate of 20 Hz(Jortner et al., 2007; Mazor & Laurent, 2005). A 20 Hz sinusoid with amplitude 0.4 times the average spiking rate was further superimposed on odor-elicited spiking to model oscillatory activity generated in the antennal lobe. Based on our own observations *in vivo* we set 10% of spontaneously active PNs to respond with inhibition to odor presentations. We used a non-homogeneous Poisson generator to create the spike trains based on these rates.

PN activity model with a shifting responsive population

To test the significance of varying temporal structure in PN firing patterns, we assumed ~30% of the PNs were unresponsive to odors, and divided the other 70% into 4 equally sized groups with the following odor-elicited sequences of excitation (E) and inhibition (I): EEI, EIE, IEI and IIE, with the last epoch occurring upon stimulus offset(Laurent & Davidowitz, 1994). Within each group, excitation epochs featured shifting sets of active PNs,

bioRxiv preprint doi: https://doi.org/10.1101/624528; this version posted May 1, 2019. The copyright holder for this preprint (which was not certified by peer review) is the author/funder, who has granted bioRxiv a license to display the preprint in perpetuity. It is made available under aCC-BY 4.0 International license.

with new PNs recruited during each LFP cycle[7]. Each group started its excitatory epoch with activation of 70% of its members and 10% were recruited in each of the next three LFP cycles. In this scheme at most ~30% of PNs were active at any given time during odor presentations.

Connectivity from GGN to KCs

Each KC received one graded inhibitory synaptic input from a randomly assigned point on GGN's calyceal branches. The strength of each synapse was adjusted to keep the KC's membrane potential close to -60 mV when bombarded by spontaneous activity from PNs, as observed *in vivo*(Joseph et al., 2012). The graded synapse was modeled as a NEURON mechanism based on published descriptions(Manor et al., 1997; Papadopoulou et al., 2011). In some simulations the individual synaptic conductances were selected from a lognormal distribution with the mean adjusted to produce realistic KC activity.

Connectivity from PNs to KCs

Half of the PN population was randomly and independently selected as presynaptic partners for each KC. If two subsets of size m and n are randomly and independently selected from a set of size q, the expected size of their intersection is $s = m * n / q$. Thus, with 800 PNs and each KC receiving input from 400 PNs, the expected number of PNs shared by any two KCs is 400 * 400 / 800 = 200, i.e., they share about 50% of their presynaptic PNs, as shown *in vivo*(Jortner et al., 2007). In some simulations the synaptic conductances were selected from a lognormal distribution with the mean adjusted to produce realistic KC activity.

IG model and connectivity

To simulate IG, we used a single compartmental Izhikevich-type model of a regular spiking (RS) pyramidal cell from the Model DB repository

bioRxiv preprint doi: https://doi.org/10.1101/624528; this version posted May 1, 2019. The copyright holder for this preprint (which was not certified by peer review) is the author/funder, who has granted bioRxiv a license to display the preprint in perpetuity. It is made available under aCC-BY 4.0 International license.

[https://github.com/ModelDBRepository/39948] modified to include graded synaptic input from GGN. To model IG's spontaneous firing, sufficient current was injected to it to generate about 7 spikes/s. A single inhibitory synapse with -80 mV reversal potential connected IG to one of GGN's basal dendrite segments. The strength and time constants for this synapse were adjusted to produce IPSP amplitudes matching those we observed *in vivo*. The same GGN segment was connected to IG via a graded synapse. In some simulations either the output of all PNs or the output of all KCs were connected to IG via excitatory synapses. The synaptic weights from KCs to IG were selected from a lognormal distribution.

Data Analysis

Most analysis and 3D visualization were carried out with custom Python scripts using published modules including numpy, scipy, networkx, matplotlib, h5py, pandas and scikitslearn.

Analyses of patch clamp recordings from KCs were carried out with custom MATLAB scripts.

Data and Software Availability

The morphological reconstruction of GGN will be made publicly available in neuromorpho repository (http://neuromorpho.org/). The morphology, electrophysiology and simulation data used in this manuscript are available at Dryad (https://doi.org/10.5061/dryad.f3t3jf0).

The code for setting up and simulating the model is available on request and will be made publicly available in ModelDB repository (https://senselab.med.yale.edu/ModelDB/). Scripts for data analysis are available at github: https://github.com/subhacom/mbnet_analysis.git.

Acknowledgements: We thank Tianming Li and Ian McBain for help with tracing GGN morphology from confocal image stacks, Nitin Gupta (IIT Kanpur, India) for providing a confocal image stack of GGN for a pilot model and helpful advice for making recordings from

bioRxiv preprint doi: https://doi.org/10.1101/624528; this version posted May 1, 2019. The copyright holder for this preprint (which was not certified by peer review) is the author/funder, who has granted bioRxiv a license to display the preprint in perpetuity. It is made available under aCC-BY 4.0 International license.

GGN. We thank the members of the Stopfer lab for feedback and suggestions and Diantao Sun and Kui Sun for excellent animal care. We also thank Vincent Schram and Lynn Holzclaw of the NICHD Microscopy Imaging Core for help with confocal imaging, George Dold and Bruce Pritchard of NIMH Section on Instrumentation for help with electrophysiology data acquisition setup, and Theodor Usdin, NIMH/NIH, for suggestions on tissue clearing and for providing initial reagents for the CUBIC protocol. We thank the Developmental Studies Hybridoma Bank for the nc82 antibody. This work utilized the computational resources of the NIH HPC Biowulf cluster. (http://hpc.nih.gov). This work was funded by an intramural grant from NIH-NICHD to M.S.

Author contributions: S.R. and M.S. designed the study. Z.A. carried out KC electrophysiology and analyzed data. S.R. carried out GGN electrophysiology, developed computational models and analyzed data. S.R. and M.S. wrote the manuscript.

Competing interests: The authors declare no competing interests.

References

Arena, P., Calí, M., Patané, L., Portera, A., & Strauss, R. (2015). Modelling the insect Mushroom Bodies: Application to sequence learning. *Neural Networks, 67*, 37-53. doi: 10.1016/j.neunet.2015.03.006

Barbour, B., Brunel, N., Hakim, V., & Nadal, J.-P. (2007). What can we learn from synaptic weight distributions? *Trends in Neurosciences, 30*(12), 622-629. doi: 10.1016/j.tins.2007.09.005

Bathellier, B., Buhl, D. L., Accolla, R., & Carleton, A. (2008). Dynamic Ensemble Odor Coding in the Mammalian Olfactory Bulb: Sensory Information at Different Timescales. *Neuron, 57*(4), 586-598. doi: 10.1016/j.neuron.2008.02.011

Bazhenov, M., Stopfer, M., Rabinovich, M., Abarbanel, H. D. I., Sejnowski, T. J., & Laurent, G. (2001). Model of Cellular and Network Mechanisms for Odor-Evoked Temporal Patterning in the Locust Antennal Lobe. *Neuron, 30*(2), 569-581. doi: 10.1016/S0896-6273(01)00286-0

Brown, S. L., Joseph, J., & Stopfer, M. (2005). Encoding a temporally structured stimulus with a temporally structured neural representation. *Nature Neuroscience, 8*(11), 1568-1576. doi: 10.1038/nn1559

Burrows, M. (1981). Local interneurones in insects. In A. Roberts & B. M. H. Bush (Eds.), *Neurons without impulses:* (1 ed., pp. 199-221): Cambridge University Press.

bioRxiv preprint doi: https://doi.org/10.1101/624528; this version posted May 1, 2019. The copyright holder for this preprint (which was not certified by peer review) is the author/funder, who has granted bioRxiv a license to display the preprint in perpetuity. It is made available under aCC-BY 4.0 International license.

Burrows, M., & Siegler, M. V. (1978). Graded synaptic transmission between local interneurones and motor neurones in the metathoracic ganglion of the locust. *The Journal of Physiology, 285*(1), 231-255. doi: 10.1113/jphysiol.1978.sp012569

Buzsáki, G., & Mizuseki, K. (2014). The log-dynamic brain: how skewed distributions affect network operations. *Nature Reviews Neuroscience, 15*(4), 264-278. doi: 10.1038/nrn3687

Cang, J., & Isaacson, J. S. (2003). In Vivo Whole-Cell Recording of Odor-Evoked Synaptic Transmission in the Rat Olfactory Bulb. *Journal of Neuroscience, 23*(10), 4108-4116. doi: 10.1523/JNEUROSCI.23-10-04108.2003

Carnevale, N. T., & Hines, M. L. (2006). *The NEURON Book* (Vol. 30).

Curtis, H. J., & Cole, K. S. (1938). Transverse Electric Impedance of the Squid Giant Axon. *The Journal of General Physiology, 21*(6), 757-765. doi: 10.1085/jgp.21.6.757

Demmer, H., & Kloppenburg, P. (2009). Intrinsic Membrane Properties and Inhibitory Synaptic Input of Kenyon Cells as Mechanisms for Sparse Coding? *Journal of Neurophysiology, 102*(3), 1538-1550. doi: 10.1152/jn.00183.2009

Eichler, K., Li, F., Litwin-Kumar, A., Park, Y., Andrade, I., Schneider-Mizell, C. M., . . . Cardona, A. (2017). The complete connectome of a learning and memory centre in an insect brain. *Nature, 548*(7666), 175-182. doi: 10.1038/nature23455

Friedrich, R. W., & Laurent, G. (2001). Dynamic Optimization of Odor Representations by Slow Temporal Patterning of Mitral Cell Activity. *Science, 291*(5505), 889-894. doi: 10.1126/science.291.5505.889

Gentet, L. J., Stuart, G. J., & Clements, J. D. (2000). Direct measurement of specific membrane capacitance in neurons. *Biophysical Journal, 79*(1), 314-320.

Gupta, N., & Stopfer, M. (2012). Functional Analysis of a Higher Olfactory Center, the Lateral Horn. *The Journal of Neuroscience, 32*(24), 8138-8148. doi: 10.1523/JNEUROSCI.1066-12.2012

Gupta, N., & Stopfer, M. (2014). A Temporal Channel for Information in Sparse Sensory Coding. *Current Biology, 24*(19), 2247-2256. doi: 10.1016/j.cub.2014.08.021

Hodgkin, A. L., & Huxley, A. F. (1952). A quantitative description of membrane current and its application to conduction and excitation in nerve. *The Journal of Physiology, 117*(4), 500-544.

Hodgkin, A. L., & Rushton, W. A. H. (1946). The Electrical Constants of a Crustacean Nerve Fibre. *Proceedings of the Royal Society of London. Series B, Biological Sciences, 133*(873), 444-479.

Inada, K., Tsuchimoto, Y., & Kazama, H. (2017). Origins of Cell-Type-Specific Olfactory Processing in the Drosophila Mushroom Body Circuit. *Neuron, 95*(2), 357-367.e354. doi: 10.1016/j.neuron.2017.06.039

Jortner, R. A., Farivar, S. S., & Laurent, G. (2007). A Simple Connectivity Scheme for Sparse Coding in an Olfactory System. *The Journal of Neuroscience, 27*(7), 1659-1669. doi: 10.1523/JNEUROSCI.4171-06.2007

Joseph, J., Dunn, F. A., & Stopfer, M. (2012). Spontaneous Olfactory Receptor Neuron Activity Determines Follower Cell Response Properties. *The Journal of Neuroscience, 32*(8), 2900-2910. doi: 10.1523/JNEUROSCI.4207-11.2012

Kay, L. M., & Stopfer, M. (2006). Information processing in the olfactory systems of insects and vertebrates. *Seminars in Cell & Developmental Biology, 17*(4), 433-442. doi: 10.1016/j.semcdb.2006.04.012

Kee, T., Sanda, P., Gupta, N., Stopfer, M., & Bazhenov, M. (2015). Feed-Forward versus Feedback Inhibition in a Basic Olfactory Circuit. *PLOS Comput Biol, 11*(10), e1004531. doi: 10.1371/journal.pcbi.1004531

Large, A. M., Vogler, N. W., Canto-Bustos, M., Friason, F. K., Schick, P., & Oswald, A.-M. M. (2018). Differential inhibition of pyramidal cells and inhibitory interneurons along the rostrocaudal axis of anterior piriform cortex. *Proceedings of the National Academy of Sciences, 115*(34), E8067-E8076. doi: 10.1073/pnas.1802428115

bioRxiv preprint doi: https://doi.org/10.1101/624528; this version posted May 1, 2019. The copyright holder for this preprint (which was not certified by peer review) is the author/funder, who has granted bioRxiv a license to display the preprint in perpetuity. It is made available under aCC-BY 4.0 International license.

Large, A. M., Vogler, N. W., Mielo, S., & Oswald, A.-M. M. (2016). Balanced feedforward inhibition and dominant recurrent inhibition in olfactory cortex. *Proceedings of the National Academy of Sciences, 113*(8), 2276-2281. doi: 10.1073/pnas.1519295113

Laurent, G. (1991). Evidence for voltage-activated outward currents in the neuropilar membrane of locust nonspiking local interneurons. *Journal of Neuroscience, 11*(6), 1713-1726. doi: 10.1523/JNEUROSCI.11-06-01713.1991

Laurent, G., & Davidowitz, H. (1994). Encoding of Olfactory Information with Oscillating Neural Assemblies. *Science, 265*(5180), 1872-1875. doi: 10.1126/science.265.5180.1872

Laurent, G., & Naraghi, M. (1994). Odorant-induced oscillations in the mushroom bodies of the locust. *J. Neurosci., 14*, 2993-3004.

Laurent, G., Seymour-Laurent, K. J., & Johnson, K. (1993). Dendritic excitability and a voltage-gated calcium current in locust nonspiking local interneurons. *Journal of Neurophysiology, 69*(5), 1484-1498.

Laurent, G., Wehr, M., & Davidowitz, H. (1996). Temporal Representations of Odors in an Olfactory Network. *The Journal of Neuroscience, 16*(12), 3837-3847.

Leitch, B., & Laurent, G. (1996). GABAergic synapses in the antennal lobe and mushroom body of the locust olfactory system. *The Journal of Comparative Neurology, 372*(4), 487-514. doi: 10.1002/(SICI)1096-9861(19960902)372:4<487::AID-CNE1>3.0.CO;2-0

Lin, A. C., Bygrave, A. M., de Calignon, A., Lee, T., & Miesenböck, G. (2014). Sparse, decorrelated odor coding in the mushroom body enhances learned odor discrimination. *Nature Neuroscience, 17*(4), 559-568. doi: 10.1038/nn.3660

Loewenstein, Y., Kuras, A., & Rumpel, S. (2011). Multiplicative Dynamics Underlie the Emergence of the Log-Normal Distribution of Spine Sizes in the Neocortex In Vivo. *The Journal of Neuroscience, 31*(26), 9481-9488. doi: 10.1523/JNEUROSCI.6130-10.2011

Luna, V. M., & Pettit, D. L. (2010). Asymmetric rostro-caudal inhibition in the primary olfactory cortex. *Nature Neuroscience, 13*(5), 533-535. doi: 10.1038/nn.2524

MacLeod, K., & Laurent, G. (1996). Distinct Mechanisms for Synchronization and Temporal Patterning of Odor-Encoding Neural Assemblies. *Science, 274*(5289), 976-979. doi: 10.1126/science.274.5289.976

Manor, Y., Nadim, F., Abbott, L. F., & Marder, E. (1997). Temporal Dynamics of Graded Synaptic Transmission in the Lobster Stomatogastric Ganglion. *Journal of Neuroscience, 17*(14), 5610-5621. doi: 10.1523/JNEUROSCI.17-14-05610.1997

Marder, E., & Goaillard, J.-M. (2006). Variability, compensation and homeostasis in neuron and network function. *Nature Reviews Neuroscience, 7*(7), 563-574. doi: 10.1038/nrn1949

Mazor, O., & Laurent, G. (2005). Transient dynamics versus fixed points in odor representations by locust antennal lobe projection neurons. *Neuron, 48*, 661-673. doi: 10.1016/j.neuron.2005.09.032

Palmer, M. J., & Harvey, J. (2014). Honeybee Kenyon cells are regulated by a tonic GABA receptor conductance. *Journal of Neurophysiology, 112*(8), 2026-2035. doi: 10.1152/jn.00180.2014

Papadopoulou, M., Cassenaer, S., Nowotny, T., & Laurent, G. (2011). Normalization for Sparse Encoding of Odors by a Wide-Field Interneuron. *Science, 332*(6030), 721-725. doi: 10.1126/science.1201835

Peng, F., & Chittka, L. (2017). A Simple Computational Model of the Bee Mushroom Body Can Explain Seemingly Complex Forms of Olfactory Learning and Memory. *Current Biology, 27*(2), 224-230. doi: 10.1016/j.cub.2016.10.054

Perez-Orive, J., Bazhenov, M., & Laurent, G. (2004). Intrinsic and Circuit Properties Favor Coincidence Detection for Decoding Oscillatory Input. *Journal of Neuroscience, 24*(26), 6037-6047. doi: 10.1523/JNEUROSCI.1084-04.2004

bioRxiv preprint doi: https://doi.org/10.1101/624528; this version posted May 1, 2019. The copyright holder for this preprint (which was not certified by peer review) is the author/funder, who has granted bioRxiv a license to display the preprint in perpetuity. It is made available under aCC-BY 4.0 International license.

Perez-Orive, J., Mazor, O., Turner, G. C., Cassenaer, S., Wilson, R. I., & Laurent, G. (2002). Oscillations and Sparsening of Odor Representations in the Mushroom Body. *Science, 297*(5580), 359-365. doi: 10.1126/science.1070502

Poo, C., & Isaacson, J. S. (2009). Odor Representations in Olfactory Cortex: “Sparse” Coding, Global Inhibition, and Oscillations. *Neuron, 62*(6), 850-861. doi: 10.1016/j.neuron.2009.05.022

Pouille, F., Marin-Burgin, A., Adesnik, H., Atallah, B. V., & Scanziani, M. (2009). Input normalization by global feedforward inhibition expands cortical dynamic range. *Nature Neuroscience, 12*(12), 1577-1585. doi: 10.1038/nn.2441

Rall, W. (1964). Theoretical significance of dendritic trees for neuronal input-output relations. In R. F. Reiss (Ed.), *Neural Theory and Modeling* (pp. 73-97). Stanford, CA: Stanford Univ. Press.

Raman, B., Joseph, J., Tang, J., & Stopfer, M. (2010). Temporally diverse firing patterns in olfactory receptor neurons underlie spatiotemporal neural codes for odors. *The Journal of neuroscience : the official journal of the Society for Neuroscience, 30*(6), 1994-2006. doi: 10.1523/JNEUROSCI.5639-09.2010

Ray, S., Chintaluri, C., Bhalla, U. S., & Wójcik, D. K. (2015). NSDF: Neuroscience Simulation Data Format. *Neuroinformatics, 14*(2), 147-167. doi: 10.1007/s12021-015-9282-5

Roth, A., & Häusser, M. (2001). Compartmental models of rat cerebellar Purkinje cells based on simultaneous somatic and dendritic patch-clamp recordings. *The Journal of Physiology, 535*(Pt 2), 445-472.

Shimizu, K., & Stopfer, M. (2017). A Population of Projection Neurons that Inhibits the Lateral Horn but Excites the Antennal Lobe through Chemical Synapses in Drosophila. *Frontiers in Neural Circuits, 11*. doi: 10.3389/fncir.2017.00030

Song, S., Sjöström, P. J., Reigl, M., Nelson, S., & Chklovskii, D. B. (2005). Highly Nonrandom Features of Synaptic Connectivity in Local Cortical Circuits. *PLoS Biol, 3*(3), e68. doi: 10.1371/journal.pbio.0030068

Stettler, D. D., & Axel, R. (2009). Representations of Odor in the Piriform Cortex. *Neuron, 63*(6), 854-864. doi: 10.1016/j.neuron.2009.09.005

Stopfer, M., Jayaraman, V., & Laurent, G. (2003). Intensity versus identity coding in an olfactory system. *Neuron, 39*, 991-1004. doi: 10.1016/j.neuron.2003.08.011

Stuart, G., & Spruston, N. (1998). Determinants of Voltage Attenuation in Neocortical Pyramidal Neuron Dendrites. *Journal of Neuroscience, 18*(10), 3501-3510. doi: 10.1523/JNEUROSCI.18-10-03501.1998

Susaki, Etsuo A., Tainaka, K., Perrin, D., Kishino, F., Tawara, T., Watanabe, Tomonobu M., . . . Ueda, Hiroki R. (2014). Whole-Brain Imaging with Single-Cell Resolution Using Chemical Cocktails and Computational Analysis. *Cell, 157*(3), 726-739. doi: 10.1016/j.cell.2014.03.042

Wüstenberg, D. G., Boytcheva, M., Grünewald, B., Byrne, J. H., Menzel, R., & Baxter, D. A. (2004). Current- and Voltage-Clamp Recordings and Computer Simulations of Kenyon Cells in the Honeybee. *Journal of Neurophysiology, 92*(4), 2589-2603. doi: 10.1152/jn.01259.2003

Zheng, Z., Lauritzen, J. S., Perlman, E., Robinson, C. G., Nichols, M., Milkie, D., . . . Bock, D. D. (2018). A Complete Electron Microscopy Volume of the Brain of Adult Drosophila melanogaster. *Cell, 174*(3), 730-743.e722. doi: 10.1016/j.cell.2018.06.019

bioRxiv preprint doi: https://doi.org/10.1101/624528; this version posted May 1, 2019. The copyright holder for this preprint (which was not certified by peer review) is the author/funder, who has granted bioRxiv a license to display the preprint in perpetuity. It is made available under aCC-BY 4.0 International license.

Figure legends

Figure 1 GGN is a very large neuron, one per hemisphere, spanning a large portion of the locust brain. (**a**) Left hemisphere: Dye filled GGN (green) in a locust brain (magenta, visualized with nc82 antibody) with an overlaid KC tracing (orange, filled in a different brain). Dorsal: towards the viewer; ventral: into the page). Right hemisphere: Circuit diagram of the locust olfactory system. Arrows show known synaptic connections, + excitatory, - inhibitory. Scale bar: 200 μm. (**b**) Very thin, feather-like neurites from GGN wrap around and penetrate the peduncle of the mushroom body, not included in our reconstruction. (**c**) GGN's neurites in the calyx have many bouton-like protrusions (**d**) whereas GGN's α lobe branches are relatively smooth. (b-d) scalebars: 100 μm. (**e**) 3D reconstruction of the same neuron shown in panel a viewed from **(i)** ventral and **(ii)** posterior side of the brain. Major branches shown in different colors. LCA: lateral calyx, MCA: medial calyx, LH: lateral horn, a: anterior, p: posterior, d: dorsal, v: ventral, l: lateral and m: medial.

Figure 2 Passive voltage spread through GGN. (**a**) Simulation schematic: GGN's α lobe branch was clamped at its stem to -40 mV (from a holding voltage of -51mV). (**b**) Conditions described in panel a lead to different steady state depolarizations of the GGN model at different locations; color indicates voltage change from resting potential; axial resistivity RA=100 Ωcm; membrane resistivity RM=33 kΩcm2. (**c**) Violin plots showing distribution of depolarization in the α lobe and the calyceal dendrites of GGN for conditions described in panel a; width of gray area indicates density, white line median, and whiskers data range. (**d**) Schematic of simulation of multiple, random synaptic inputs to GGN: 500 synapses were connected to GGN's α lobe branch. (**e**) Bottom: raster plot of incoming spike times at all 500 synapses. The spikes arrived at each synapse at random times at linearly decreasing rate, starting with 20/s down to 0 after 500 ms. Top: for conditions shown in panel d, membrane potentials at randomly sampled terminal neurites in different regions of GGN. (**f**) Violin plots of peak depolarizations in the α lobe dendrites and the calyceal dendrites in model

bioRxiv preprint doi: https://doi.org/10.1101/624528; this version posted May 1, 2019. The copyright holder for this preprint (which was not certified by peer review) is the author/funder, who has granted bioRxiv a license to display the preprint in perpetuity. It is made available under aCC-BY 4.0 International license.

described in panel d. (**g**) Violin plots of distribution of depolarizations in the calyx for different values of axial resistivity (RA, bottom) and membrane resistivity (RM, right) for the voltage clamp simulation described in panel a. Lines connect the median results for specified RMs (right).

Figure 3 Feedback inhibition from GGN extends the dynamic range of KCs. (**a**) Model schematic: A single KC sends 50,000 excitatory synapses with random delays of 0-60 ms into GGN's α lobe branch. The KC receives feedback inhibition via a graded synapse from GGN's calyceal branch. A step current is injected into the KC from 500-3000ms (the end of simulation). (**b**) Comparison of membrane potential evoked by current pulses of different amplitudes in isolated KC (left) and KC with feedback inhibition (right). As the amplitude of the current pulse increases, the KC's spiking first increases, and then, as the membrane potential nears saturation, decreases. (**c**) Comparison of the number of spikes evoked in KC with and without feedback inhibition during the 2500 ms current step.

Figure 4 *In vivo,* GGN's responses to odors vary with odor and animal. Examples from 3 animals and 2 odors (horizontal gray bars, 1 s) (black traces: average of 5 trials, gray: standard error of the mean, data low-pass filtered at 49 Hz). Response features include depolarization or hyperpolarization upon stimulus onset and/or offset, and depolarization or hyperpolarization evoked by different odors in the same GGN.

Figure 5 Tuning the olfactory network by reference to GGN's olfactory responses required heterogeneous synaptic strengths onto KCs and structured patterns of activity in PNs, predicting a small proportion of hyperactive KC responses. **(a)** Schematic of mushroom body network model. Each of the 50,000 KCs receives input from 50% of the 830 PNs, which are modeled as spike trains. All KCs excite GGN in its α lobe branch and receive inhibition from a random calyceal branch of GGN. **(b-d)** Model with simplified, homogenous firing patterns in PNs and uniform synaptic strengths generates unrealistic membrane potential in GGN. **(b)** Raster plot of model PN spike trains (67 shown); dots in each row mark spike times in a PN.

bioRxiv preprint doi: https://doi.org/10.1101/624528; this version posted May 1, 2019. The copyright holder for this preprint (which was not certified by peer review) is the author/funder, who has granted bioRxiv a license to display the preprint in perpetuity. It is made available under aCC-BY 4.0 International license.

(c) Raster plot of spike trains evoked in the KCs (397 shown) when all of them receive identically strong inhibitory connections from GGN. **(d)** Unrealistic membrane potential in GGN features a few peaks corresponding to highly synchronized bouts of activity in KCs. **(e-f)** Model in which subpopulations of PNs have different temporal patterns of spiking during and after odor stimulation generates unrealistic membrane potential in GGN. **(e)** Rasters show different firing patterns in different PNs. **(f)** Simulation of model with PN activity pattern in panel e and uniform synaptic strengths onto KCs generates unrealistic membrane potential in GGN. **(g)** Simulated membrane potential of GGN in a model with both structured PN activity patterns in panel e and heterogeneous synaptic strengths gives rise to sustained depolarization of GGN similar to that observed *in vivo* (e.g. Figure 4 animal 1). Dark gray bar: 1 s odor stimulation; light gray bar: 200 ms “off response” period. **(h)** Histogram of KC firing rates in the network model giving the realistic result shown in panel g; odors evoke in most KCs 0-2 spikes/s, but in a few KCs higher firing rates.

Figure 6 *In vivo*, some KC responses are hyperactive, as predicted. **(a)** KC firing rate averaged over 707 KC-odor pairs. Shaded region indicates standard error of the mean. Black horizontal bar: 1 s odor stimulation. **(b)** A hyperactive response KC filled with dye (mushroom body calyx and pedunculus outlined with dashed lines (scale bar: 50 μm) and **(c)** its recorded membrane potential in response to odor stimulus, and **(d)** its average firing rate elicited by this stimulus. **(e)** Histogram of average number of spikes in KCs across trials upon odor presentation.

Figure 7 An additional, unidentified olfactory pathway to IG is needed to explain odor-elicited hyperpolarization in GGN. **(a)** *In vivo* recordings of GGN’s membrane potential from two animals showing IPSPs (arrowheads) believed to originate as spikes in IG. Vertical scale bar: 10 mV. **(b)** Peristimulus time histogram (PSTH) shows IPSP peak times from 1257 odor-trials across 47 GGNs, presumably reflecting spikes in IG. Black horizontal bar: odor presentation in panels a and b, which share the time axis. **(c)** Same as panel b but showing full responses. **(d)** Schematic of model with IG receiving direct excitation from KCs and

bioRxiv preprint doi: https://doi.org/10.1101/624528; this version posted May 1, 2019. The copyright holder for this preprint (which was not certified by peer review) is the author/funder, who has granted bioRxiv a license to display the preprint in perpetuity. It is made available under aCC-BY 4.0 International license.

reciprocal inhibition with GGN. **(e)** Top: simulated GGN membrane potential including odor-elicited hyperpolarization mimics responses observed *in vivo* (e.g. Figure 4, Animal 3, hexanal). Bottom: corresponding simulated IG membrane potential. This simulation included a 200 ms synaptic delay from KCs to IG. The PN activity patterns were like those shown in Figure 5. **(f-g)** Varying the temporal pattern of PN population activity can produce different response pattern in the same network as e. **(f)** Raster plot of PN activity with a different temporal pattern from that in e. **(g)** Top: simulated GGN membrane potential including odor evoked de- and hyperpolarization (similar to Figure 4, Animal 1 hexanal). Bottom: corresponding simulated IG membrane potential. **(h)** Spontaneous activity in IG does not originate in the antennal lobe. Top two black traces show spontaneous IPSPs in GGN's membrane voltage from two animals with intact olfactory systems. The bottom two red traces are from the left and the right GGN in another animal in which the antennal lobes had been silenced by cutting both antennal nerves. Vertical scale bar 5 mV, horizontal scale bar 1 s.

Figure 8 Updated olfactory connectivity model where odor responses in the KC population are gated by feedback inhibition from GGN and inhibition of GGN via odor evoked spiking in IG, which itself receives input from an unknown olfactory pathway.

Supplemental Information

Video S1. Related to Figure 1: 3D view of the confocal stack of the dye filled GGN in Figure 1a.

Video S2. Related to Figure 2: 3D view of depolarizations (color coded spheres) at various locations in GGN arbor in simulation described in Figure 2a.

Figure S3. Related to Figure 2: KC activity vs GGN voltage deflection in simulations where all KCs received identical PN input. ▬ GGN->KC maximum conductance 0.7 nS and PN-

bioRxiv preprint doi: https://doi.org/10.1101/624528; this version posted May 1, 2019. The copyright holder for this preprint (which was not certified by peer review) is the author/funder, who has granted bioRxiv a license to display the preprint in perpetuity. It is made available under aCC-BY 4.0 International license.

> KC maximum conductance 3.7 pS, GGN->KC maximum conductance 0.5 nS and PN-> KC maximum conductance 3.7 pS, GGN->KC maximum conductance 0.9 nS and PN-> KC maximum conductance 4.0 pS, GGN->KC maximum conductance 0.9 nS and PN-> KC maximum conductance 4.5 pS. GGN segments were grouped by peak depolarization from resting potential and the total number of spiking KCs postsynaptic to these segments (top) or the total number of spikes in the KCs postsynaptic to these segments (bottom) were normalized by the total number of spiking and nonspiking KC post synaptic to these segments.

Figure S4. Related to Figure 5: Model with steady activity in a fixed set of PNs (as in Figure 5b) can produce sustained depolarization of GGN when the synaptic strengths are lognormally distributed. Gray: 1 s odor stimulus.

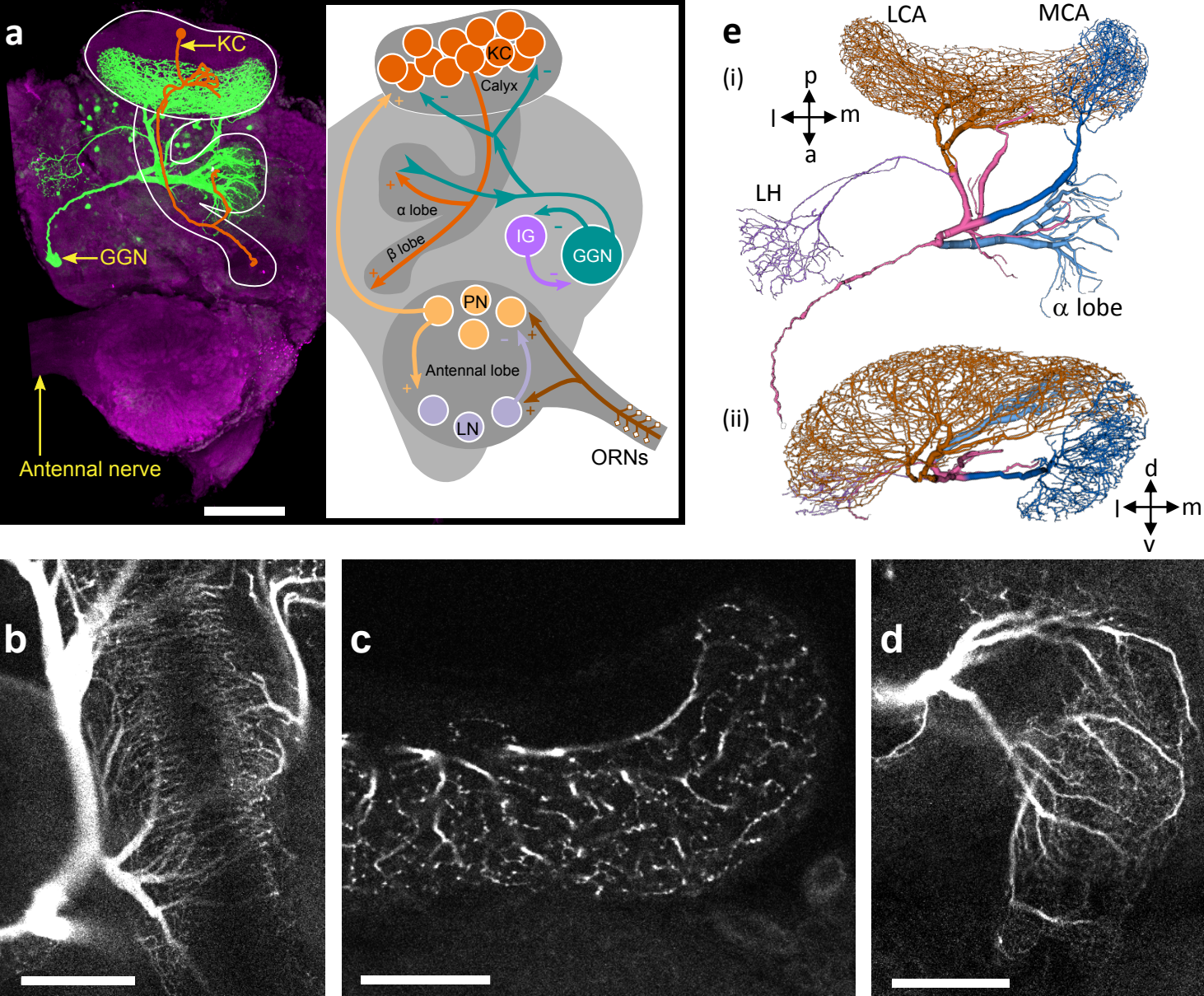
a
KC
GGN
Antennal nerve
KC
Calyx
α lobe
β lobe
IG
GGN
PN
Antennal lobe
LN
ORNs
e
LCA
MCA
(i)
p
l
m
a
LH
α lobe
(ii)
d
l
m
v
b
c
d

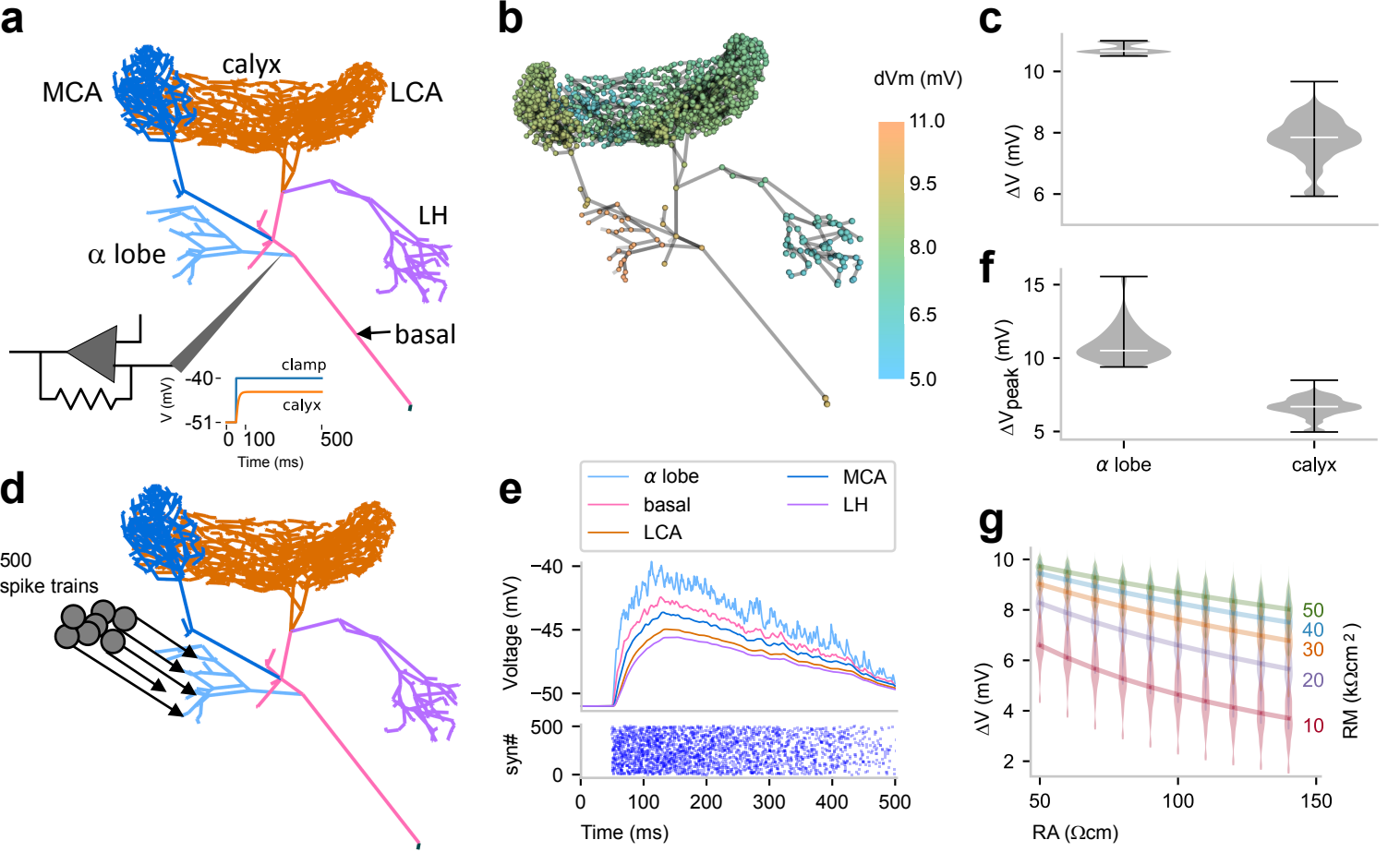
a
MCA
calyx
LCA
LH
α lobe
basal
clamp
calyx
-40
-51
V (mV)
0
100
500
Time (ms)
b
dVm (mV)
11.0
9.5
8.0
6.5
5.0
c
ΔV (mV)
10
8
6
f
ΔVpeak (mV)
15
10
5
α lobe
calyx
d
500
spike trains
e
α lobe
basal
LCA
MCA
LH
Voltage (mV)
−40
−45
−50
syn#
500
0
0
100
200
300
400
500
Time (ms)
g
ΔV (mV)
10
8
6
4
2
50
100
150
RA (Ωcm)
50
40
30
20
10
RM (kΩcm 2)

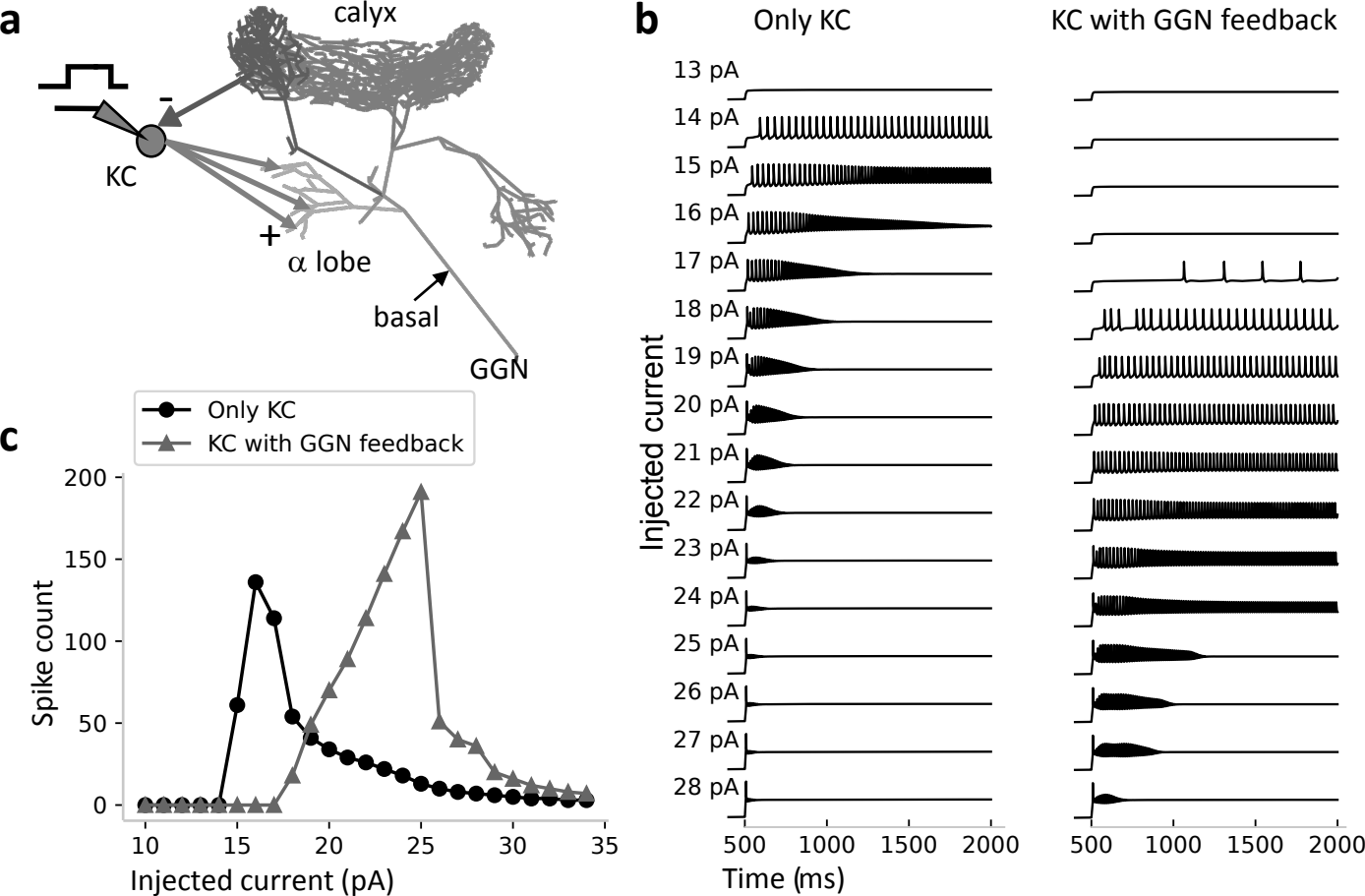
a
calyx
KC
-
+
α lobe
basal
GGN
b
Only KC
KC with GGN feedback
13 pA
14 pA
15 pA
16 pA
17 pA
18 pA
19 pA
20 pA
21 pA
22 pA
23 pA
24 pA
25 pA
26 pA
27 pA
28 pA
Injected current
500
1000
1500
2000
Time (ms)
c
Only KC
KC with GGN feedback
Spike count
200
150
100
50
0
10
15
20
25
30
35
Injected current (pA)

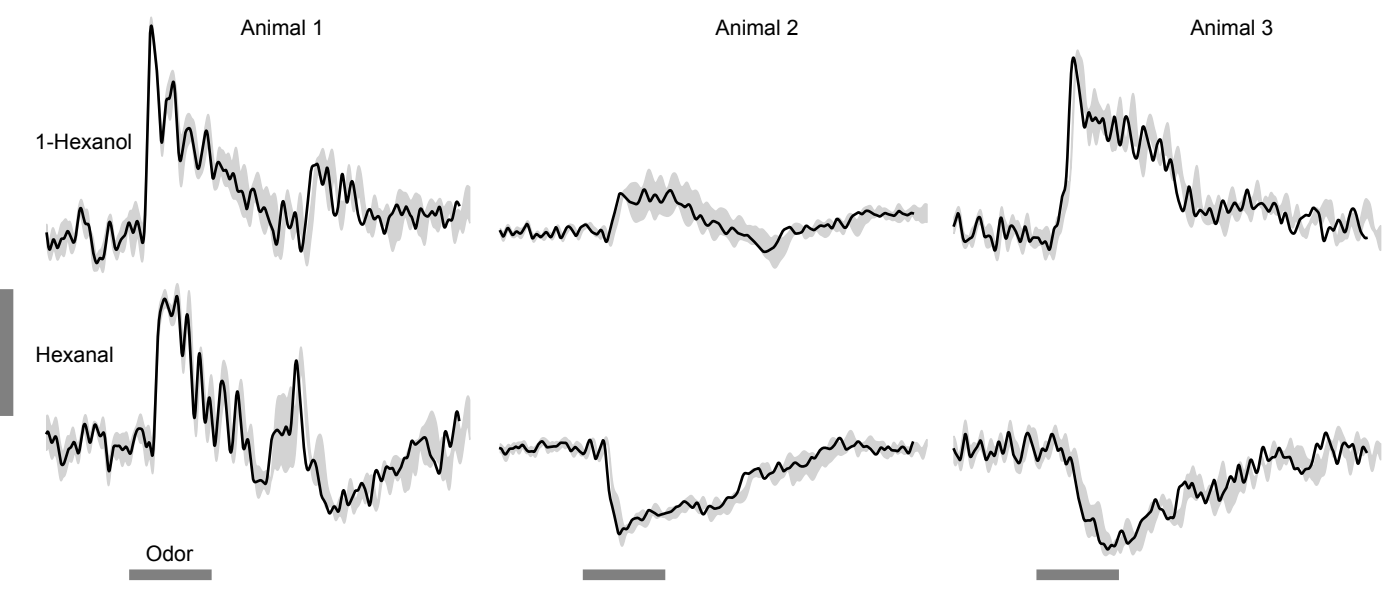
Animal 1
Animal 2
Animal 3
1-Hexanol
Hexanal
Odor

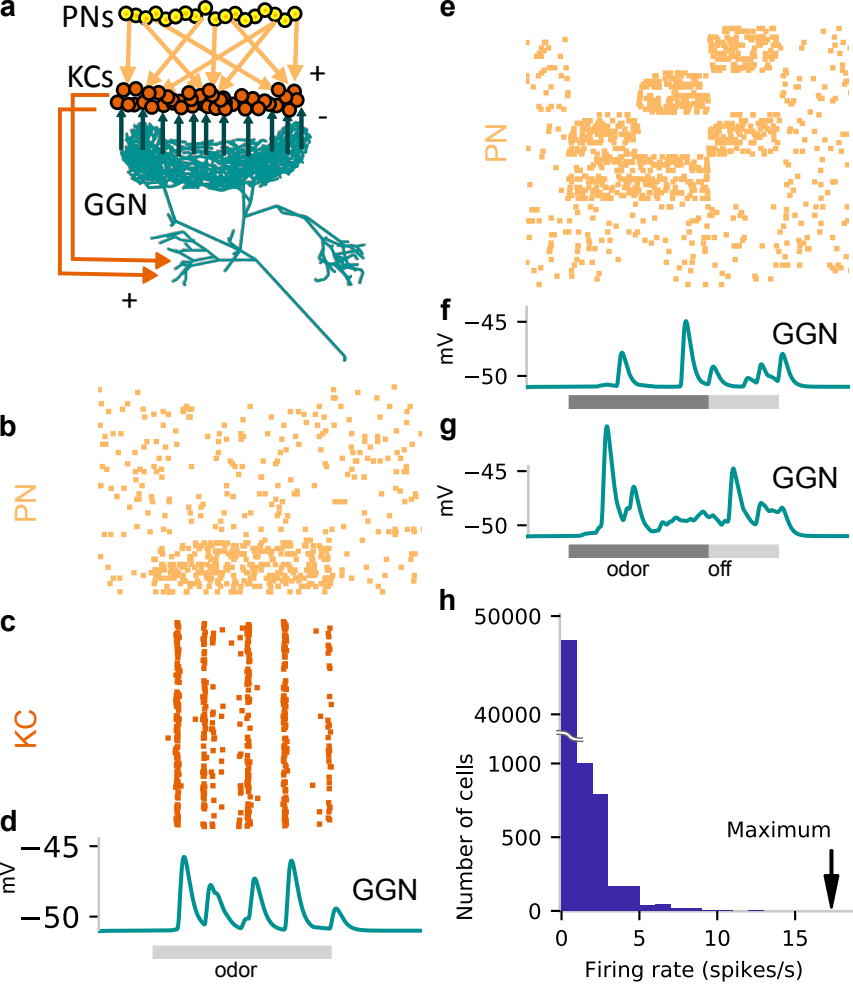
a
PNs
KCs
+
-
GGN
+
b
PN
c
KC
d
mV
−45
−50
GGN
odor
e
PN
f
mV
−45
−50
GGN
g
mV
−45
−50
GGN
odor
off
h
50000
40000
1000
500
0
Number of cells
Maximum
0
5
10
15
Firing rate (spikes/s)

bioRxiv preprint doi: https://doi.org/10.1101/624528; this version posted May 1, 2019. The copyright holder for this preprint (which was not certified by peer review) is the author/funder, who has granted bioRxiv a license to display the preprint in perpetuity. It is made available under aCC-BY 4.0 International license.

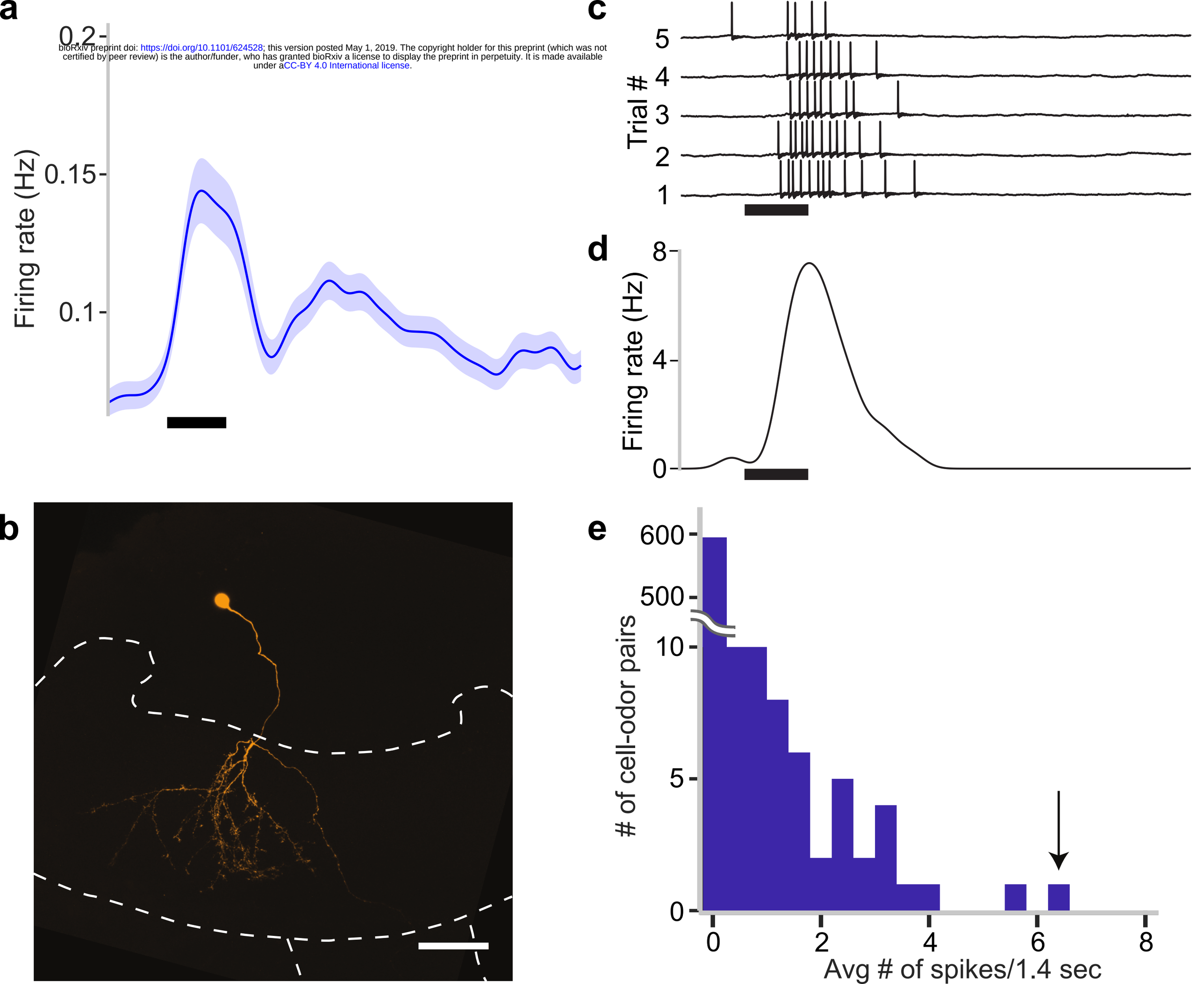

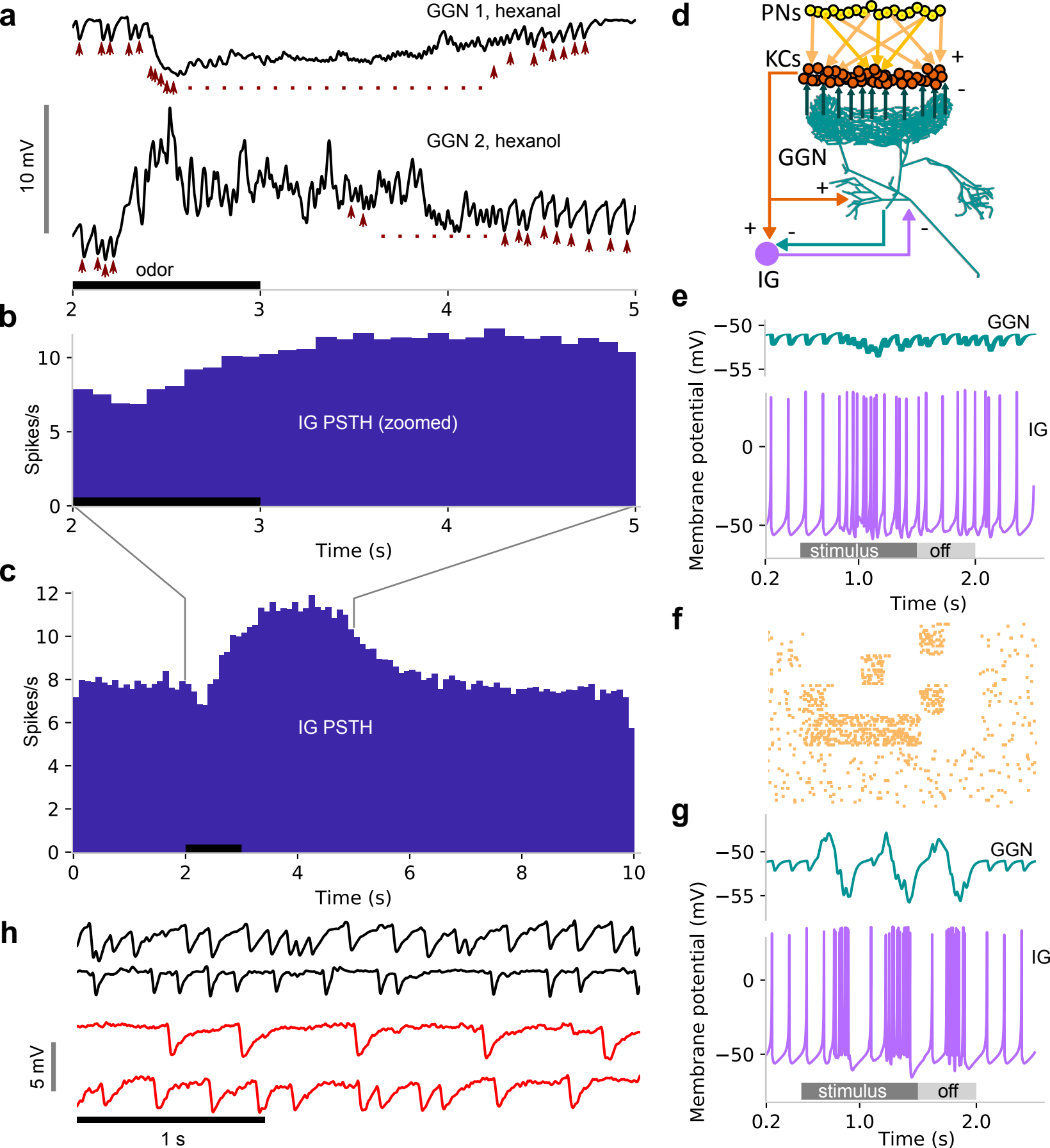
a
GGN 1, hexanal
GGN 2, hexanol
10 mV
odor
2
3
4
5
b
IG PSTH (zoomed)
Spikes/s
Time (s)
c
IG PSTH
Spikes/s
Time (s)
d
PNs
KCs
GGN
IG
e
GGN
IG
Membrane potential (mV)
stimulus
off
Time (s)
f
g
GGN
IG
Membrane potential (mV)
stimulus
off
Time (s)
h
5 mV
1 s

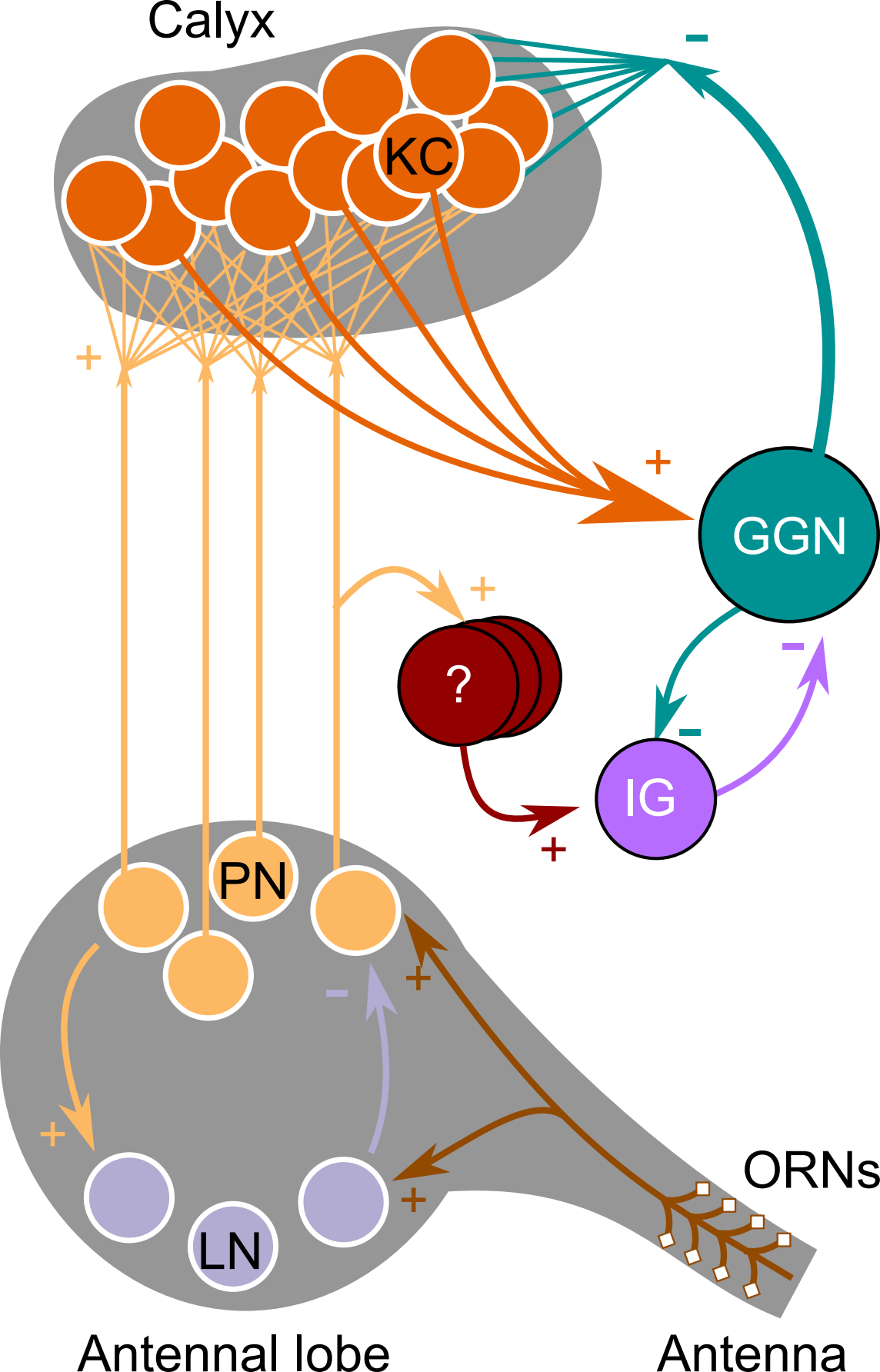
Calyx
KC
GGN
?
IG
PN
LN
ORNs
Antennal lobe
Antenna

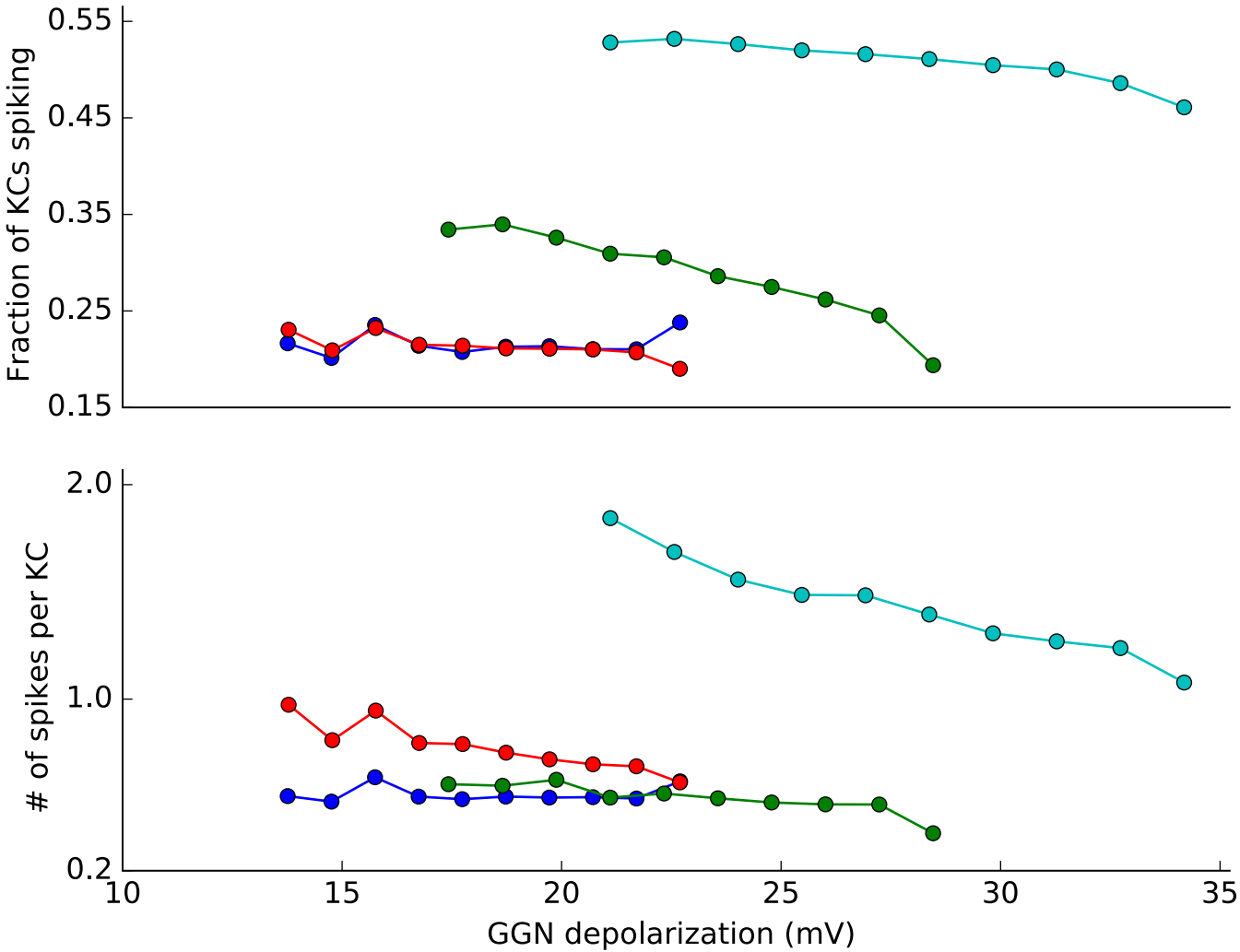
Fraction of KCs spiking
0.55
0.45
0.35
0.25
0.15
# of spikes per KC
2.0
1.0
0.2
10
15
20
25
30
35
GGN depolarization (mV)

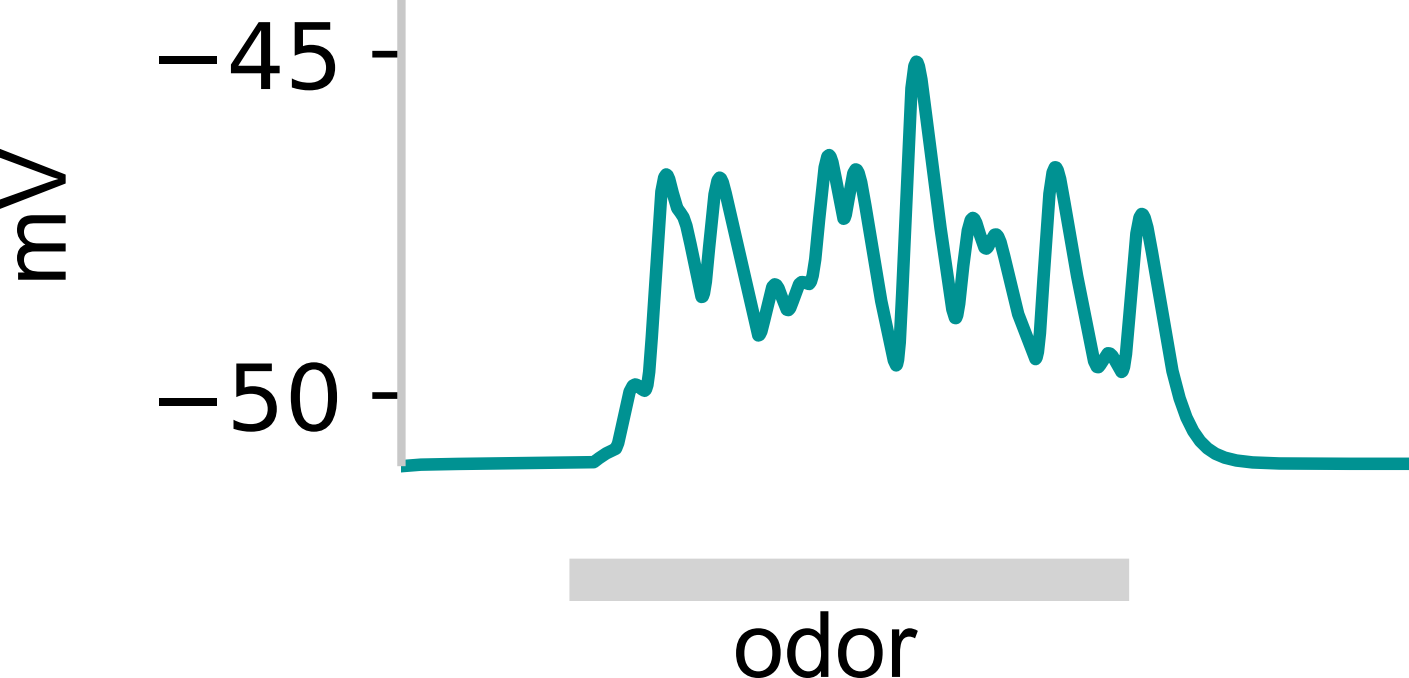
−45
−50
mV
odor